Rowe et al., Multi-proxy speleothem record of climate instability during the early last interglacial in southern Turkey

Highlights

- A speleothem from Turkey provides a climate record through Termination II;
- Isotopic evidence shows rainfall increased at the start of the last interglacial;
- A dry period lasting ~200 years occurred early in the last interglacial;
- The isotopic structure of the dry event is similar to the Holocene 8.2 ka event;
- A synchronous climate anomaly is identified in other European speleothems;

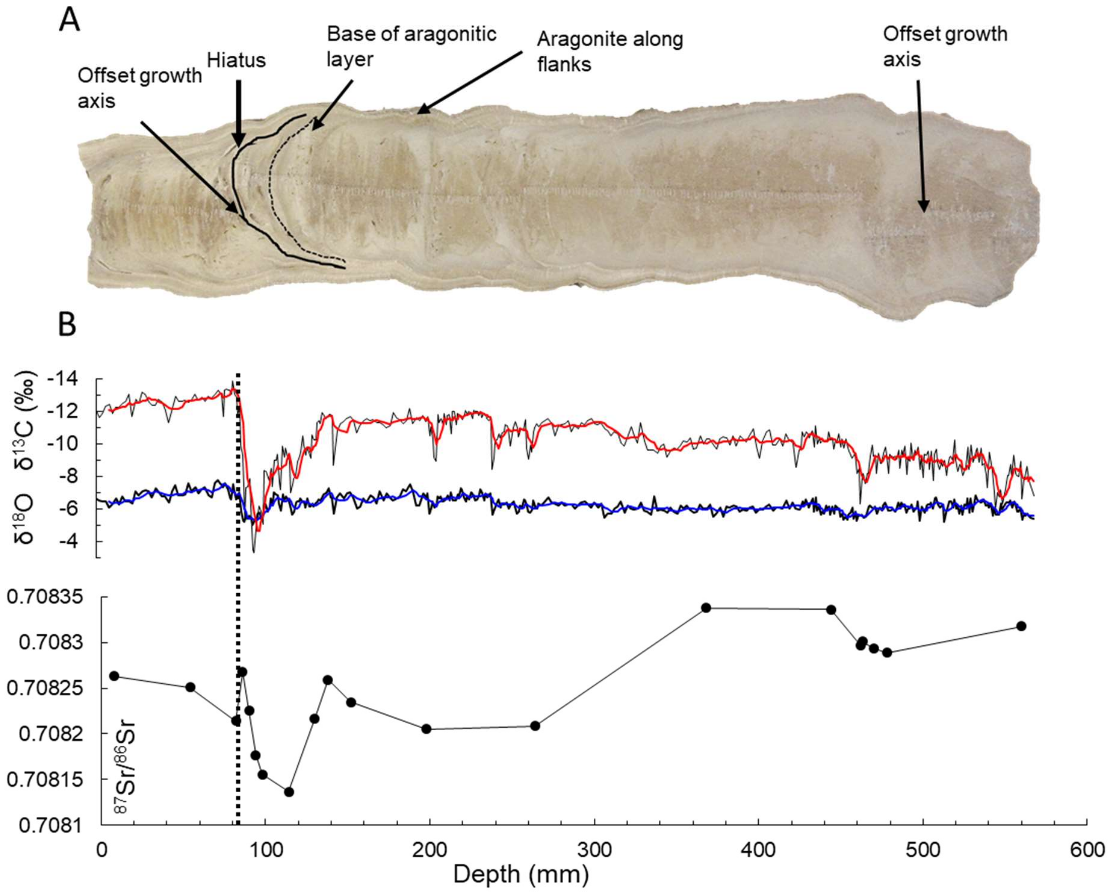

A
Offset growth axis
Hiatus
Base of aragonitic layer
Aragonite along flanks
Offset growth axis
B
δ18O δ13C (‰)
-14
-12
-10
-8
-6
-4
87Sr/86Sr
0.70835
0.7083
0.70825
0.7082
0.70815
0.7081
0
100
200
300
400
500
600
Depth (mm)

Multi-proxy speleothem record of climate instability during the early last interglacial in southern Turkey

Rowe, P.J.[1*], Wickens, L. B.[1], Sahy, D.[2], Marca, A. D.[1], Peckover, E.[1], Noble, S.[2], Özkul, M.[3], Baykara, M. O.[3], Millar I.L[2], and Andrews, J.E.[1]

[1] School of Environmental Sciences, University of East Anglia, Norwich NR4 TJ, UK.

[2]Geochronology and Tracers Facility, NERC Isotope Geosciences Laboratory, British Geological Survey, Keyworth, Nottingham NG12 5GG, UK

[3] University of Pamukkale, Department of Geology, 20070, Denizli, Turkey

*Corresponding Author: p.rowe@uea.ac.uk

Declarations of Interest: None

Abstract: A stalagmite from Dim Cave in southern Turkey contains a climate record documenting rapid and significant changes in amounts of precipitation between ~132 ka and ~128 ka, during the penultimate glacial – interglacial transition. Some U-Th dates have been compromised by carbonate dissolution but rigorous selection and tuning to $\delta^{18}O$ records from other speleothems has generated a robust age model. Growth rate was initially very slow but a rapid increase at ~129 ka was accompanied by strong negative trends in $\delta^{18}O$ and $\delta^{13}C$, a combination implying the onset of much wetter conditions. Isotopic values at ~129 ka suggest that groundwater recharge rates and biogenic activity in the soil zone exceeded those of the early Holocene. A significant isotopic enrichment event at ~128 ka, during which there was alternating aragonite and calcite deposition, documents a strong drying event with a duration that lasted ~200 years. A concurrent decrease in $^{87}Sr/^{86}Sr$ ratios indicates increased groundwater residence times and the cumulative evidence suggests amounts of rainfall fell from well above to slightly below present-day levels. Similar $\delta^{18}O$ enrichment events are present in coeval speleothem records from southwest France and the Northern Alps, and these, together with pollen evidence from Italy, Greece and the Iberian margin of drier conditions at this time, imply that a climate anomaly extended across the northern Mediterranean borderlands. The timing, duration and structure of this episode are consistent with marine evidence of strong North Atlantic cooling early in the last interglacial and there is a resemblance to the Holocene 8.2 ka event recorded globally in many proxy-climate archives.

Keywords: Stalagmite; Termination II; stable isotopes; climate anomaly; aragonite; Mediterranean.

1. Introduction

Glacial to interglacial transitions involve complex changes in climate on decadal to millenial timescales as large land-based northern hemisphere ice sheets disintegrate, raising sea level and stimulating changes in ocean and atmosphere circulation patterns. The nature and timing of climate changes during the Late Glacial - Early Holocene transition in the North Atlantic region is known in considerable detail from multiple sources (Lowe et al., 2008) such as high resolution stable isotope data from Greenland ice cores (Steffensen et al., 2008) and lacustrine cores (Von Grafenstein et al., 1999), palynological profiles (Allen et al., 1999; Bottema, 1995; Lotter et al., 2000), coleopteran records (Coope and Lemdahl, 1995; Coope et al., 1998) and marine sediment cores (McManus et al., 2004; Peck et al., 2008).

These have identified rapid switching between stadial and interstadial conditions prior to the start of the Holocene at 11.7 ka (Walker et al., 2009) as erratic ice sheet disintegration periodically disrupted the North Atlantic meridional overturning circulation (MOC), with consequent strong and widespread impacts on global climates. In contrast, the penultimate transition into the last interglacial (LIG), between ~132 ka and ~128 ka, is known in less detail, mainly because the Greenland record does not extend beyond the mid-LIG (Andersen et al., 2004), fewer high resolution terrestrial sites of relevant age survive for study and chronologies are generally less well constrained. These limitations compromise both the detection of short-lived climatic events in many terrestrial palaeoclimate archives, and their correlation with possible equivalents in the more complete marine records.

In the Mediterranean, the penultimate glacial-interglacial transition is recorded in diverse proxy-climate records including stable isotopes and growth rates in speleothems (Bar-Matthews et al., 2003; Drysdale et al., 2009), lacustrine palynological profiles (Allen and Huntley, 2009; Brauer et al., 2007; Milner et al., 2012; Sinopoli et al., 2018; Tzedakis, 2003), variations in shelf sediment flux (Toucanne et al., 2015) and multi-proxy marine core data (Grant et al., 2012; Jimenez-Amat and Zahn, 2015; Kandiano et al., 2014; Martrat et al., 2014; Rohling et al., 2015). A general trend towards more negative $\delta^{18}O$ values is generally seen in Mediterranean speleothems through the transition, a pattern which is linked via atmospheric water vapour of predominantly marine origin to a similar trend in ocean water due to rising sea levels (Rohling et al., 2015). Concurrent increases in speleothem growth rates (Drysdale et al., 2009) imply higher groundwater infiltration rates and soil pCO_2 as a consequence of increasing rainfall between ~132 ka - 128 ka stimulated by rising sea surface temperatures (SST) (Kandiano et al., 2014; Martrat et al., 2004). A strengthening African Summer Monsoon increased freshwater outflow from the River Nile and North African wadi systems, contributing substantially to the formation of Sapropel S5 at ~129 ka (Grant et al., 2012; Ziegler et al., 2010). It has been suggested that freshwater input to the Mediterranean was dominated by African sources and that additional contributions were negligible (Osborne et al., 2010), and some modelling simulations suggest that Eemian European storm tracks were shifted further north than at present (Kaspar et al., 2007). However, there is also evidence of a significant runoff contribution from the Mediterranean northern borderlands (Rohling et al., 2015; Toucanne et al., 2015) which has been linked to increased winter rains in the Mediterranean during periods of precession minima (Bosmans et al., 2015; Kutzbach et al., 2014). Pollen evidence shows that Mediterranean sclerophyllous vegetation increased and peaked very early in the LIG, demonstrating that summers were hot and dry and therefore that increased rainfall was confined to the winter months (Milner et al., 2012), implying an Atlantic moisture source for the precipitation rather than an incursion of summer monsoonal air from the south. Marine records from the North Atlantic indicate significant instability in the MOC during the glacial-interglacial transition (Irvali et al., 2012; Mokeddem et al., 2014; Nicholl et al., 2012), and this is likely to have stimulated abrupt changes in atmospheric circulation patterns downstream over Eurasia. Identification and high resolution capture of such rapid climate events in contemporary terrestrial archives is currently limited, although there has been recent progress towards integrating marine, pollen and speleothem data into a coherent climatic framework (Tzedakis et al., 2018).

Here we use oxygen, carbon and strontium isotope data, together with petrography, from a speleothem from Dim Cave in southern Turkey to infer changes in rates of groundwater recharge through the penultimate glacial-interglacial transition. These changes imply significant variability in climate, especially in rainfall, similar to early-mid-Holocene fluctuations which are linked to instability in the North Atlantic MOC (Cheng et al., 2009b; Daley et al., 2011).

2. Cave setting and regional climate

Dim Cave (36º 32’ 27” N, 32º 06’ 32” E) is located 235 metres above sea level in a spur on the southern wall of the Dim River valley ~6 km from the Mediterranean coast of southern Turkey, 11 km east of Alanya and 145 km south-east of Antalya (Fig. 1). It is a linear fault-controlled fossil phreatic cave formed in dolomitised Permian limestone which constitutes the upper unit of the Alanya Nappe (Okay and Ozgul, 1984). The single main passage ~360 m long and 10-15 m wide, shows considerable vertical development along fissures, and terminates in a small subterranean lake which is perched on a bed of impermeable schist. Shoreline evidence suggests that the lake level has previously been ~0.5 m higher. The epikarst varies in thickness from a few metres to several tens of metres and is overlain by thin soils which support a mainly coniferous woodland with an understorey of bushes and a sparse ground cover. The dominant vegetation units of the region are generally red pine and maquis (Kurt et al., 2015). Relative humidity in the cave is >90 % (Baykara, 2014) and the temperature is 18-19ºC, indistinguishable from the average annual mean 1963-2004 temperature of 18.4ºC at the coastal station of Antalya, 130 km WNW of Dim Cave and 50 m above sea level (IAEA/WMO), and from temperatures in Soreq Cave (385 m a.s.l.), Israel, and winter-spring SST in the Eastern Mediterranean (EM) (Bar-Matthews et al., 2003). Although the cave is richly decorated, much of it is presently dry with seepage waters restricted to a few locations mainly associated with major fissures. Modern active straw stalactites selected for analysis were 100% aragonite (identified by X-ray diffraction, XRD), implying that under present conditions this is the dominant speleothem-forming mineral. This contrasts with the predominantly calcite mineralogy of the speleothems from the cave used to reconstruct a continuous climate record for the period 90 – 10 ka during which aragonite was only recorded between ~80 – 75 ka (Unal-Imer et al., 2015; Ünal-Imer et al., 2016).

Turkey lies in a zone of transition between the mid-latitude westerlies and the sub-tropical high pressure belt, which dominate in winter and summer respectively, and its climatology is complex (Spanos et al., 2003). In southern Turkey, as in most of the Mediterranean, summers are very dry and there is a pronounced winter rainfall maximum. Atlantic depressions reach the Eastern Mediterranean through Western and Central Europe and via the Western Mediterranean Basin and regenerate in centres of cyclogenesis located in the Gulf of Genoa, the Aegean and off southern Cyprus (Alpert et al., 1990; Karaca et al., 2000; Krichak and Alpert, 2005; Kutiel et al., 2002; Türkeş, 1998; Türkeş et al., 2008). The intensity and tracks of winter depressions, and therefore rainfall amounts, are influenced by regional pressure patterns, primarily the North Atlantic Oscillation (NAO) (Türkeş and Erlat, 2003), an Eastern Atlantic-Western Russian (EAWR) pressure pattern (Krichak and Alpert, 2005) and a North Sea-Caspian Pattern (NSCP) (Kutiel and Benaroch, 2002). Consequently, winter rainfall amounts in the EM are ultimately determined by regional circulation patterns beyond the Mediterranean Basin.

Antalya receives over 70% of its annual rainfall (~1100 mm) between November and February and 98% between October and May (Fig. S1). The mean November – February $\delta^{18}O$ value from intermittent Antalya precipitation data from 1963 – 2004 is -5.8±0.6‰$_{VSMOW}$ (IAEA/WMO), identical to the mean $\delta^{18}O$ value of -5.7±0.3‰$_{VSMOW}$ from five sets of six drip and pool water samples collected from Dim Cave and a nearby large spring in March, May and December 2009 and January and February 2010. These plot along a meteoric water line (MWL) (Fig S2) defined by

$$\delta^2H = 7.0 \cdot \delta^{18}O + 14.2. \quad (1)$$

This compares with

$$\delta^2H = 7.3 \cdot \delta^{18}O + 12.9 \quad (2)$$

for Antalya monthly precipitation 1963-2001 (Dirican et al., 2005), and

$$\delta^2H = 7.2 \cdot \delta^{18}O + 10.8 \quad (3)$$

for groundwaters on the windward (southern) side of the Taurus Mountains (Schemmel et al., 2013). The lower slope of Dim Cave water may indicate some mixing with a residual element of evaporated water within the epikarst. The proximity of the data to the Mediterranean Meteoric Water Line (MMWL)

$$\delta^2H = 8.0 \cdot \delta^{18}O + 22 \quad (4)$$

rather than the Global Meteoric Water Line (Fig S2) points to the Mediterranean as the principal moisture source for the seepage waters. The Antalya and Taurus Mountain meteoric water lines are intermediate between the global and Mediterranean lines, probably indicating a significant contribution from moisture sources beyond the Mediterranean Basin. Incomplete monthly data for Antalya from 1963 to 2004 suggest that $\delta^{18}O$ in precipitation declines by about 0.8‰ per 200 mm of rainfall, compared with 1.0±0.1‰ per 200 mm at Soreq Cave, Israel from twelve years of annual data (Bar-Matthews et al., 1997) and 1.6±0.2‰ per 100 mm reported for monthly data from the Central Mediterranean (Bard et al., 2002). This negative relationship between $\delta^{18}O$ in precipitation and rainfall amount (the "amount effect" (Dansgaard, 1964)) is generally considered to strongly influence $\delta^{18}O$ in Mediterranean speleothems on sub-orbital timescales.

3. Materials and Methods

3.1 Speleothem Description

Dim 1 is a fossil stalagmite, 568 mm long and between 110 and 180 mm in diameter (Fig. 2a). Dim 1 toppled before 8.0 ka, as it has a small aragonite stalagmite (Dim 3; mineralogy from XRD) on its upper side which grew between 8.0 and 7.0 ka (Table 1), and it was missing its top and several mm of its base when collected. Longitudinal sectioning revealed discrete growth layers. A growth axis offset of ~5 mm occurs at 460 mm distance from top (dft), and at 259 mm and 131 mm dft the axial laminae flatten to define obvious 'stalagmite top' morphologies. This is particularly clear at 131 mm dft where the stalagmite top was rimmed by 'edge ramparts' that defined a <5 mm deep pool (Fig. 2b). There is no evidence that growth stopped at any of these morphological surfaces. A prominent band of paler, creamy carbonate is present between 103 and 87 mm dft (Fig. 2b) and this carbonate can be followed into flanking layers that encase the 'core' of the speleothem (Fig. 2b). In the axial part of the stalagmite, at 87 mm dft, the upper surface of this pale, creamy carbonate band displays a clear corrosion surface interpreted as a hiatus (Fig. 2b). Above this surface there is a 10 mm zone where pale creamy carbonate near the flanks appears to be replaced by darker carbonate in the axial zone (Fig. 2b). Moreover, above the corrosion surface the growth axis is offset by ~20 mm. The speleothem diameter narrows slightly towards the top and culminates in a broken surface.

3.2. U-Series Dating

Twenty five 100-150 mg samples were taken for U-series dating using a hand-held drill. All were proximal to the central growth axis except 52-1, -2, -3, -4 and -5 which were taken from the flanking pale creamy-coloured aragonite layers that could be traced into the growth axis, except 52-3 which stratigraphically was a few mm higher (Fig. 2a). Laboratory and instrumental methods are detailed in Supplementary Material.

3.3. Carbonate $\delta^{18}O$ and $\delta^{13}C$ analyses

421 carbonate samples each weighing ~70 µg were drilled at 1 or 2 mm intervals along the growth axis using a 0.5 mm hand-held dental drill. The measurements were carried out in the Stable Isotope Laboratory at the University of East Anglia, UK, on a Europa SIRA II dual inlet isotope ratio mass spectrometer following reaction with 100% phosphoric acid at 90º C, using an on-line 'common acid bath' system. An internal laboratory standard ($\delta^{13}C$ = 1.99‰$_{VPDB}$, $\delta^{18}O$ = -2.05‰$_{VPDB}$) calibrated against NBS19 ($\delta^{13}C$ = 1.95‰$_{VPDB}$, $\delta^{18}O$ = -2.20‰$_{VPDB}$) was measured with the samples in each batch. Measurement precision based on the standard deviation of repeat analyses of the standard (n=7) was better than 0.08‰ for both oxygen and carbon. Isotopic data are recalculated to an acid reaction temperature of 25ºC and aragonite $\delta^{18}O$ values corrected by -0.29‰ to account for the differing calcite and aragonite acid fractionation factors (Lachniet, 2015). Final values are reported as parts per thousand (‰) deviations relative to VPDB.

3.4. Strontium isotope analysis

Strontium isotope analyses were carried out at the NERC Isotope Geosciences Facility, Keyworth, UK. Samples were taken adjacent to the growth axis and leached in 1% acetic acid in order to remove labile strontium. Samples were then leached in warm 10% acetic acid in order to dissolve carbonate material. The first batch of samples were not spiked, but subsequent samples were spiked with an ^{84}Sr tracer to allow calculation of the Sr concentration in addition to the isotope composition. Following conversion to nitrate, Sr was separated using EICHROM Sr-Spec ion exchange resin, loaded on single Re filaments using a TaO activator, and analysed using a Thermo Scientific Triton mass spectrometer operating in multi-dynamic mode. Nine analyses of the NBS987 standard gave a value of 0.710251 ± 0.000003 (4.9 ppm, 1-sigma) at the time of analysis.

4. Results

4.1. Petrography

Dim 1 has a mixed mineralogy of calcite and aragonite as identified petrographically and confirmed by X-ray diffraction. Axial parts of Dim 1 are mainly inclusion-poor columnar calcite, but are encased by flanks of pale creamy-pink aragonite-rich layers (Fig. 2a). These flanking layers thin and pinch out downward, and above ~88 mm dft they thicken and project above the broken stalagmite top (Fig. 2b). Detailed relationships between these aragonite-rich flanking layers and the axial part of the stalagmite are described after the more obvious changes in the axial part have been outlined.

The axial stalagmite 'core' consists largely of grey-brown columnar compact (C) calcite, which in some places have length to width ratios approaching the elongated columnar (Ce) fabric (Fig. 3a) of (Frisia, 2015). Toward the edges of the calcite 'core', C fabrics can grade into, or inter-finger with, pale cream columnar open (Co) fabrics (Frisia, 2015), a relationship similar to that described in a speleothem from Jeita Cave, Lebanon (Verheyden et al., 2008). These paler Co calcites also extend across most of the width of the axial 'core' at depths of

119-133 mm and 201-204 mm dft, and contain columnar crystals with shorter c-axes than the grey-brown C calcites.

At ~103 mm dft there is a prominent, sharp, boundary with millimetre-scale, step-like relief forming a central 'horst', followed by a 7 to 13 mm zone of mixed aragonite and calcite alternating in millimetre-scale layers grading into mainly aragonite on the flanks. This is the pale creamy zone seen in slabbed specimen (Fig. 2b). In the axial part of Dim 1 where the isotope transect was drilled, the first 2.0 mm of this zone is dominantly (90%) bundles of acicular aragonite that nucleated directly on underlying columnar crystal terminations with c-axes normal to stalagmite extension direction (Fig. 3b); spaces between bundles are filled with non-orientated aragonite needles (Fig. 3c). At topographic highs on this boundary the C calcites of the central 'horst' show sharp lateral change to aragonite (Figs. 3c and d). The next 4 mm are dominantly (>90%) calcitic C fabrics which then grade back to a layer of pure aragonite needles 2 mm thick (Fig. 4a). A 1 mm thick C calcite (100%) layer follows (Fig. 4a), and above this pure aragonite needle fabrics return for 1.5 mm with sharp but irregular upper boundary that in places cuts out the entire aragonite layer into the underlying 1 mm thick C calcite layer. The vertical transition between aragonite and calcite in this zone is not always sharp and the layer thicknesses given above vary laterally over centimetre-scale distances with the calcite layers wholly replaced by aragonite in some places. Within this zone there are multiple horizons of linear inclusions arranged parallel to growth that occur in both the aragonite and calcite fabrics, in the latter often associated with isolated aragonite needles (Fig. 4b and c).

On the flanks of this zone the mineralogy is almost purely aragonite, present up to 0.5 mm lower than the basal boundary in the axial part. The aragonite fabrics are dominantly acicular bundles or spherulitic aggregates of needle crystals (Fig. 4d) with a highly irregular upper boundary (Fig. 5a). At the boundary, calcite C crystals or more mosaic fabrics about the aragonite needle fabrics (Fig. 5a).

The upper boundary of the mixed mineral zone in the axial 'core' (~87 mm dft; Fig. 4b and c) is sharp but undulose with underlying crystals showing ragged terminations (Fig. 4c). Above this, the growth axis is offset and stalagmite diameter reduces. Above the upper boundary, pale cream Co calcite is the dominant fabric, although in places directly above the boundary the basal 200-500 μm contains patchy equant microspar fabrics (Fig. 4c).

At depths of 9 mm, 36 mm, 103 mm, 114 mm, 120 mm, 143 mm and 262 mm dft, thin horizons of aragonite project into the axial calcite zone from the flanking layers but typically die out before reaching the axis. These horizons have sharp lower and upper boundaries and pass laterally into sub-horizontal, undulose, dark 'lines' (<1 μm thick), usually inclusion-rich and parallel to growth in the central axis (Fig. 5b-e). The fluid inclusions are typically spherical (Fig. 5c) and range in size between <1 μm and 15 μm. Some, but not all, of these dark lines and inclusion trails are associated with relict aragonite needles (Fig. 5d); some grade laterally into darker and thicker layers (mean ~70 μm) that define crystal terminations (Fig. 5e) and in places appear to corrode the underlying calcite. These dark lines and layers occur at irregular intervals along the stalagmite but are not necessarily defined by inclusion trails or confined to locations where remnants of aragonite persist.

4.2. Uranium-series

The U-series data (Table 1) reveal negligible levels of ^{232}Th, U concentrations in aragonite that are 10-60 times higher than in calcite, and calculated ages between 117 ka and 137 ka (Figs. S3, S4). However, the dates do not consistently lie in stratigraphic order, implying a degree of isotopic mobility in some samples. This is most likely related to the dark "lines" and fluid inclusion trails identified at intervals within the stalagmite (Section 6, below) and which are often associated with corrosion of underlying crystal terminations. Petrographic examination shows the presence of such features at sample locations 29-10, 41-8, 41-6, 29-7, 41-5, 41-4, 33-6, 41-2, 41-1 and 33-5, (Table 1).

4.3. Oxygen and carbon isotopes

The $\delta^{18}O$ and $\delta^{13}C$ profiles (Fig. 6a, b) are broadly similar (linear regression of the two data sets yields $r^2 = 0.47$), although the latter shows a stronger overall negative trend, and both capture a strong positive excursion beginning at ~143 mm dft and culminating in the hiatus at 87 mm dft, following the switch from calcite to predominantly aragonite deposition. Minimum $\delta^{18}O$ and $\delta^{13}C$ values occur above the hiatus, after which they increase towards the broken stalagmite top. $\delta^{18}O$ values below 240 mm dft lie mainly between -5.5‰ and -6.5‰, falling subsequently to between -6.5‰ and -7.0‰ before increasing rapidly above 140 mm to a maximum of -5.0‰ at 95 mm dft within the aragonite-rich layer. Above the hiatus $\delta^{18}O$ values around -7.8‰ gradually increase to -6.5‰ at the broken top. Typically, the values in Dim 1 are ~0.5‰ more negative than those recorded in Dim Cave speleothem E2 between 13 ka and 10 ka during the last glacial-interglacial transition (Unal-Imer et al., 2015). In comparison, aragonite from modern straw stalactites and mid-Holocene stalagmite Dim 3 have $\delta^{18}O$ values between -3.6‰ and -5‰. The structure of the carbon isotope record shows a more distinct negative drift from the base to 140 mm dft than the oxygen. $\delta^{13}C$ values in the lower 100 mm lie mainly around -9‰, comparable to those recorded in Dim Cave speleothems between 13.0 ka and 11.5 ka (Unal-Imer et al., 2015), and fall to -11.5‰, similar to early Holocene, in two step-wise depletions at ~460 mm and ~320 mm dft, although several brief ~3‰ positive excursions also occur within this phase. Above ~140 mm $\delta^{13}C$ increases erratically to a maximum of -3.3‰ at 96 mm depth within the mixed mineralogy zone. Immediately above the hiatus, values of around -13.8‰ rise to -12‰ at the broken stalagmite top. These are lower than in modern straw stalagmites (-7‰ to -10‰), and in Dim 3 where values increase from between -6.5‰ and -8.0‰ at ~8.0 ka to -3.4‰ at ~6.9 ka.

Five of the eleven isotope samples in the zone of mixed mineralogy immediately below the hiatus at 87 mm dft (Fig. 2b) are aragonite and three have mixed mineralogy. Theoretical calculations and experimental and empirical evidence indicate that $\delta^{18}O$ in aragonite is enriched by about 0.8‰ relative to calcite precipitating from the same parent water (Fohlmeister et al., 2018; Grossman and Ku, 1986; Kim et al., 2007; Tarutani et al., 1969). Four of the five aragonites in Dim 1 are isotopically lighter than two of the calcite samples and a 0.8‰ correction generates implausibly high data scatter compared to the coherent non-corrected structure (Fig. 6a). Consequently, no adjustment has been applied to the aragonite $\delta^{18}O$ values. $\delta^{13}C$ enrichments in aragonite of 1.0‰ - 2.5‰ relative to calcite have been reported from several locations (Frisia et al., 2002; Holmgren et al., 2003; McMillan et al., 2005; Morse and Mackenzie, 1990; Romanek et al., 1992), and recent analysis identified an offset of 1.16±0.46‰ (Fohlmeister et al., 2018). However, to remain consistent with the $\delta^{18}O$ data, the aragonite $\delta^{13}C$ values have also not been modified.

4.4. Strontium Isotopes

$^{87}Sr/^{86}Sr$ ratios (Fig. 6c) are primarily influenced by the local limestone ($^{87}Sr/^{86}Sr$ = 0.70716) and overlying soil ($^{87}Sr/^{86}Sr$ = 0.70845), although regional sources such as sea spray and far travelled aeolian dust are also potential contributors (Zhou et al., 2009) (Fig. 7). Speleothem values lie on a mixing line, one end member of which is the limestone bedrock and the other a composite source with a ratio higher than that of the soil (Fig. 7) (Supplementary Material). Ratios in Dim 1 are comparable to those measured in the Mid-Holocene Dim 3 speleothem (0.70821-0.70827) although encompassing a greater range, and rather lower than modern soda straws which have a composition similar to modern overlying soil. The $^{87}Sr/^{86}Sr$ pattern along the speleothem shows an abrupt fall between 370-260 mm depth and a sharp drop at 140-115 mm immediately followed by a rapid increase (Fig. 6c).

5. Discussion and Interpretation

5.1. Petrography

Columnar compact (C) fabrics are primary calcites that tend to form in thin water films with slow drip rates and enhanced degassing under well-ventilated conditions (Frisia, 2015), while transition to columnar open (Co) fabrics may suggest progressively less efficient degassing, probably as water film depth increases (Kendall and Broughton, 1978). In temperate climates C fabrics form under low (up to 0.35) $CaCO_3$ saturation states and low drip water Mg concentrations (Mg/Ca ratio <0.3) (Frisia and Borsato, 2010). However, the tendency toward Ce fabrics also suggests that Mg/Ca ratios were at times >0.35 (Frisia, 2015) and possibly above 0.85 (Gonzalez et al., 1992).

Aragonite in the mixed-mineral axial zone shows little evidence of preserved dissolution-reprecipitation fabrics indicative of neomorphic alteration (Frisia, 2015; Frisia and Borsato, 2010; Martín-García et al., 2019). Rather, aragonite growth directly off the underlying C crystals and abundant evidence of both lateral and vertical transitions from C calcite into acicular aragonite (Fig. 4a) suggest concurrent competitive growth (A. Kendall, pers. com., 2015), i.e. co-precipitation of both polymorphs (McMillan et al., 2005; Railsback et al., 1994; Spötl et al., 2002). Lateral polymorph co-precipitation, and vertical switching between aragonite and calcite is likely controlled by variations in Mg/Ca ratios close to the calcite inhibition threshold (Frisia et al., 2002; Riechelmann et al., 2014; Rossi and Lozano, 2016) albeit probably 'conditioned' by low parent water $CaCO_3$ supersaturation state (De Choudens-Sánchez and Gonzalez, 2009). Variable rates of groundwater recharge through the dolomitised epikarst would achieve the required variations in drip water MgCa ratios. The presence of acicular aragonite indicates very low drip rates (Frisia, 2015), usually indicating relatively dry conditions. The predominance of aragonite, and its spherulitic morphology, in the flank areas of Dim 1 relative to the axial part suggests that increasing fluid Mg/Ca ratios resulting from axial calcite precipitation (Fairchild et al., 2000) may influence aragonite precipitation, although enhanced evaporation of the flanking water film could also have been a factor (Railsback et al., 1994).

The down-cutting nature of both the lower and upper boundaries to the mixed-mineral layer and the ragged aragonite crystal terminations below the upper boundary indicate corrosion and dissolution. Patchy presence of calcite microspar immediately above this boundary is probably a remnant dissolution-reprecipitation fabric (see e.g. (Frisia et al., 2002)) although the lateral impersistence of the microspar suggests that, mostly, neomorphic alteration fabrics were wholly removed by dissolution, followed by later precipitation of primary Co calcites.

The only other place where calcite fabrics are clearly neomorphic is in the flanking aragonites (Fig. 5a).

The presence of inclusions in an otherwise inclusion-poor stalagmite implies some disruption to the normal growth conditions which were largely not conducive to trapping water, perhaps because of almost perfect crystal coalescence on the crystal growth surfaces (Kendall and Broughton, 1978). Some linear inclusion trails in C calcites are associated with relict aragonite needles, which are interpreted as partial dissolution fabrics followed by calcite regrowth largely as a primary precipitate, entombing aragonite relics. Dissolution of primary aragonite near the growth axis was thus common, and inclusion trails contained within calcite crystals adjacent to preserved aragonite layers almost certainly mark the position of former aragonite layers. Typically, the inclusion-rich horizons are undulose, a geometry probably deriving from unevenly corroded crystal edges. The thicker, darker, sub-horizontal lines are also interpreted as dissolution surfaces as shown by the etching and corrosion of underlying calcite crystal terminations. These dissolution-precipitation phases probably mainly represent seasonal to sub-decadal events rather than significant breaks in growth.

5.2. U-series Systematics

5.2.1 Age Model

The age inversions (Table 1, Fig. S3) most likely result from U-series decay chain disruption due micro-scale corrosion events in the axial zone, caused by aggressive drip waters, which have been identified at several horizons. Five samples (the 52-series in Table 1) were taken from discrete pristine aragonite layers on the flanks of Dim 1 which could be traced into the growth axis (except 52-3 which narrowly post-dates the broken stalagmite top), although some are replaced in the axial zone by a dissolution horizon where aragonite has been removed. This approach was possible only in the upper part of Dim 1 where the aragonite layers are sufficiently thick, and four samples lie stratigraphically above the hiatus at 87 mm dft and one below (52-5). Whilst not in strict stratigraphic order, the dates all overlap at 2 s.d. (average 128.3±0.4 ka), suggesting rapid speleothem growth at this time. No petrographic evidence has been found indicating likelihood of isotopic disturbance in these aragonites. Furthermore, differential U isotope mobility in a suite of samples in which U concentrations vary by up to a factor of six would be likely to generate considerable age scatter, and it is highly improbable that samples subjected to any significant disturbance could still return such convergent ages. Therefore, although limited U mobility cannot be discounted, the 52-series (aragonite) dates are likely to closely represent the true sample ages.

Since the 52-series (aragonite) dates establish the age of the upper part of the speleothem as ~128 ka (Table 1), it follows that the stalagmite must be older than this below 96 mm depth and that the ten dates younger than 127.2 ka (the lower 2σ limit of 52-2) can confidently be rejected (Fig. S3). Significantly, these ten dates are from sample locations which petrographic evidence of linear surfaces and inclusion planes show to have been subject to episodic corrosion (Table 1). Sample 29-9 (136.2 ka), which is clearly an outlier, is also rejected. An age model has therefore been constructed from the remaining fourteen dates using StalAge (Scholz and Hoffmann, 2011) and this additionally rejects 37-3 (130.5 ka) as an outlier (Fig. 8). No geochemical or petrographic grounds have been identified on which to reject any of the final 13 dates used in the age model, which is considered to reliably represent the speleothem chronology within the errors of the method. Following a period of slow growth (~30 mm ka^{-1}) from ~132 ka, a very rapid growth rate of ~400 mm ka^{-1} is implied for the upper part of the speleothem, almost as fast as the rates recorded in speleothem CC5 from Corchia Cave at around 128 ka (Drysdale et al., 2009). The duration of the prominent hiatus at 87 mm depth cannot be resolved by the aragonite dates and hence was less than the 2σ dating errors (~0.7 ka, see also Section 5.5) and it has been disregarded in the construction of the age model.

The general validity of this model is supported by evidence from $(^{234}U/^{238}U)_0$ ratios (Fig. 9) which fall from ~2.0 near the base of the speleothem to a plateau of ~1.4 at about 168 mm depth, similar to the mid-Holocene values of Dim 3 (1.284 to 1.302). Although some calculated ages are in error by up to ~8% (Table 1), resultant $(^{234}U/^{238}U)_0$ values are modified by <1%. This declining pattern resembles that from speleothems from Israel that grew over the past 25 ka and which showed simultaneous reductions in both $(^{234}U/^{238}U)_0$ and $\delta^{18}O$ as rainfall increased through the transition from the last glacial into the Holocene (Kaufman et al., 1998). A similar correspondence is seen in Dim 1 (Fig. 9), which is consistent with speleothem growth commencing at a time when groundwater was passing through weathered but unleached soils and epikarst after a dry phase, followed by preferential removal of ^{234}U from recoil-damaged sites under wetter conditions, leading to a subsequent gradual reduction in $(^{234}U/^{238}U)_0$. $\delta^{18}O$ data from Corchia Cave (Drysdale et al., 2009) and Tana che Urla Cave (TCU) (Regattieri et al., 2014) show that warm and wet conditions were established in southern Europe by ~131.5 ka and stable isotope values in Dim 1 when growth commenced are similar to those recorded from Dim Cave for the Pleistocene-Holocene transition (Unal-Imer et al., 2015). This suggests that Dim 1 started growing at a time of climatic transition and the basal date of ~132 ka is compatible with that inference and also with the observed pattern of $(^{234}U/^{238}U)_0$ evolution, since Marine Isotope Stage (MIS) 6, like MIS 2, was a period of relative aridity.

5.2.2. U-Th Open System Processes

The U-Th isotope disruption in Dim 1 is most likely related to redistribution of high U concentrations from discrete aragonite horizons following their partial dissolution soon after deposition, and a notable feature is that nine of the eleven rejected ages are lower than predicted by the age model. An investigation into the impact of diagenetic alteration, including post-depositional dissolution, on U-Th speleothem ages has identified circumstances in which infiltration waters could potentially corrode speleothem carbonate (Scholz et al., 2014). These are (1) mixing corrosion caused by two or more saturated solutions becoming under-saturated w.r.t. calcite on mixing; (2) pCO_2 in the cave atmosphere being higher than in the soil zone; (3) seepage waters failing to reach saturation w.r.t. carbonate due to high infiltration rates; (4) uptake of CO_2 by seepage waters from the cave atmosphere following their isolation from the soil atmosphere under closed system conditions. The first two conditions require a cave to be poorly ventilated, which is unlikely in this case since Dim Cave has a relatively large natural entrance. But condition (3), and perhaps (4), could occur periodically on decadal to centennial timescales in the wet winter-dry summer climate of the Eastern Mediterranean. Speleothem surfaces could suffer leaching by aggressive drip waters following either torrential autumn-winter rains, or substantial lowering of groundwater storage levels in the epikarst. Some recent studies have examined the effects of later diagenetic replacement of aragonite by calcite on U distribution (Domínguez-Villar et al., 2017; Martín-García et al., 2019), and the likely role of micro-voids as pathways for U migration during aragonite to calcite conversion was identified in a speleothem from Corchia Cave, northwest Italy (Bajo et al., 2016). There, modelling showed that early conversion of even small percentages of (high U) aragonite to (low U) calcite in

LIG speleothems can increase apparent ages by $10^3 - 10^4$ ka. In contrast, the rejected dates in Dim 1 are mainly younger than their true ages as predicted by the age model. Microprobe analyses of speleothems from a cave in the Pyrenees documented U redistribution during aragonite to calcite transformation, and U/Th dating returned ages both older and younger than expected, possibly implicating thorium migration (Ortega et al., 2005). An age 10 ka less than predicted was also recorded in a mixed-mineral speleothem from Morocco at an aragonite-calcite transition (Wassenburg et al., 2012). Despite these valuable studies, the behaviour of U-Th isotopes under open-system conditions in speleothems remains poorly understood and the specific processes controlling isotopic redistribution in Dim 1 are unclear, although early aragonite dissolution is strongly implicated. No replacement of aragonite by calcite is evident from petrographic analysis, and U loss is unlikely to be a significant factor given the dominance of lower, rather than higher, calculated ages relative to age model estimates.

5.3. Controls on oxygen and carbon isotopes

5.3.1. Oxygen isotopes.

Climatic controls on speleothem $\delta^{18}O$ are complex (Lachniet, 2009; McDermott, 2004) particularly at times of global transition from glacial to interglacial states when the ocean-atmosphere system undergoes significant reorganisation, as during the period of Dim 1 deposition. Mediterranean stalagmites typically record decreases of 1‰ to 4‰ through this time period (Bar-Matthews et al., 2003; Drysdale et al., 2009; Regattieri et al., 2014), dominated by the negative $\delta^{18}O$ trend in ocean source water (Marino et al., 2015; Rohling et al., 2015), and increasing rainfall (the “amount effect”) as a consequence of a strengthening hydrological cycle (Bar-Matthews et al., 2003; Bard et al., 2002; Dansgaard, 1964; Drysdale et al., 2009; Regattieri et al., 2014; Rowe et al., 2012; Unal-Imer et al., 2015; Zanchetta et al., 2014). Modelling studies have identified a particularly strong connection between higher SST in the EM and increased precipitation over the Anatolian Peninsula (Bozkurt and Sen, 2011). Once marine surface water $\delta^{18}O$ values stabilised at interglacial values, the amount effect became the principal driver of high frequency variability in speleothem $\delta^{18}O$ signals. In a climate with strongly seasonal rainfall, fluctuating precipitation amounts in winter are likely to dominate Mediterranean speleothem $\delta^{18}O$ records, which therefore become sensitive recorders of changes in local water balance. Periods of reduced winter rainfall generate isotopically enriched groundwater and elevated $\delta^{18}O$ in speleothem carbonate, and may create a negative water balance in semi-arid regions leading to evaporation in the unsaturated zone and enhanced isotopic enrichment (Markowska et al., 2015). Winter rainfall amounts in Turkey are strongly influenced by depression track trajectories, which are steered by regional pressure patterns (Dirican et al., 2005; Kutiel et al., 2002; Saris et al., 2010; Türkeş and Erlat, 2003), and hence Eastern Mediterranean speleothem $\delta^{18}O$ profiles are related to changes in regional atmospheric circulation. Changes in air mass trajectories have been invoked as long term controls on isotopes in precipitation in the Eastern Mediterranean (Unal-Imer et al., 2015).

5.3.2. Equilibrium Deposition

The average $\delta^{18}O$ composition of a large pool, the cave lake and drip waters from five sites collected during 2009-2010 was -5.7±0.3‰$_{VSMOW}$ (Fig. S2). This compares with -6.2‰ for water from a large spring just below the cave, which probably receives flow from higher catchments inland from the cave. The predicted equilibrium value for aragonite precipitating from the cave waters at 18-19ºC is about -5.7‰$_{PDB}$ (Kim et al., 2007), whereas the average $\delta^{18}O$ compositions of two active aragonite straw stalactites from Dim Cave are -4.2±0.1‰ $_{PDB}$ (n=6) and -4.4±0.1‰$_{PDB}$ (n=6). When plotted as 1000lnα vs $10^{3}T^{-1}$, the stalactite data lie above aragonite–water equilibrium lines which have been determined experimentally (Grossman and Ku, 1986; Kim et al., 2007) (Fig. S5a). Empirical data from speleothem calcite-water measurements (Tremaine et al., 2011) are not consistent with the experimentally derived calcite-water equilibrium relationship commonly used in speleothem studies (Kim and O'Neil, 1997), and it may be the case that water-carbonate fractionation factors for speleothems are higher than the calculated experimental values (Coplen, 2007; Dietzel et al., 2009) (Fig. S4A). It has been proposed that a "window of equilibrium" may exist for aragonite deposits in the zone ±0.5‰ either side of computed aragonite-water equilibrium lines (Lachniet, 2015). The Dim stalactites are enriched by ~1.4‰ and therefore lie beyond this limit (Fig. S5B) and modern aragonite deposits in Dim Cave appear not to be forming in equilibrium with seepage waters. Hendy Tests (Hendy, 1971) were carried out along growth layers at 277 mm, 94 mm (within the aragonitic layer) and 22 mm depth. These show only weak correlations between $\delta^{18}O$ and $\delta^{13}C$, no systematic enrichment of $\delta^{18}O$ away from the growth axis and $\delta^{18}O$ variability along growth layers not exceeding 0.6‰ (Fig. S6) and may suggest that kinetic fractionation during the early LIG, under different hydrological conditions, was rather limited. The weaknesses of this test are, however, widely acknowledged (Dorale and Liu, 2009; Fairchild et al., 2006; Lachniet, 2009, 2015) and it is probable that proximity to equilibrium deposition varied temporally as hydrological conditions changed.

5.3.3. Carbon isotopes.

$\delta^{13}C$ values in speleothems are strongly influenced by the intensity of biogenic activity in the soil zone above the cave, but may be modified by processes within the epikarst prior to the emergence of seepage water into the cave atmosphere (Fairchild et al., 2006; McDermott, 2004). Root respiration, organic matter decay and microbial activity in densely vegetated soils generate CO_2 containing isotopically light carbon, which in areas dominated by C3 plants will typically yield speleothem $\delta^{13}C$ values of -8‰ to -14‰ (Dorale et al., 1992; Hendy, 1971). Less negative values (-6‰ to +2‰) may indicate reduced biogenic-derived CO_2 due to sparser vegetation cover and/or a greater contribution from isotopically heavier atmospheric CO_2 and carbonate bedrock (Genty et al., 2003) or, in certain regions, a higher proportion of C4 plants (Baker et al., 2002). However, rapid CO_2 degassing of groundwater and/or evaporation in air-filled voids above the cave can lead to prior calcite precipitation (PCP) (Fairchild et al., 2000), also resulting in carbon isotope enrichment of calcite along the deposition pathway and ultimately in higher speleothem $\delta^{13}C$ values (Frisia et al., 2011). Such local, site-specific, factors can significantly increase both the frequency and amplitude of carbon isotope variability in a speleothem relative to coeval oxygen isotope data, which may dilute the impact and increase the ambiguity of the $\delta^{13}C$ climate signal.

5.4. The Penultimate Deglaciation in the Mediterranean

Growth in Dim 1 began around ~132.0 ka, broadly coinciding with trace element evidence of increasing rainfall at TCU Cave in northern Italy (Regattieri et al., 2016), and continued through the latter part of the penultimate glacial-interglacial transition. The stable isotope data show an erratic pattern of increasingly negative values into the early LIG (Fig. 10a,b) in common with other speleothem records from the Mediterranean region, NW Europe and China which document all or part of the transition (Fig. 11c,d,e). Marine SST and $\delta^{18}O$, which strongly influence speleothem $\delta^{18}O$ signals, also show marked variability over this time period (Fig. 11f,g,h). There are inherent difficulties in integrating marine and speleothem chronologies, and thus in directly correlating terrestrial and marine records (Govin et al., 2015), but the strong hydrological links between marine source waters and speleothems have been utilised to synchronise land and marine archives (Drysdale et al., 2009), and to refine marine chronologies (Jimenez-Amat and Zahn, 2015; Marino et al., 2015). Between ~132.1 ka and ~130.2 ka, $\delta^{18}O$ values in Dim 1 oscillate between -5.5‰ and -6.5‰ on centennial timescales with declining amplitude (Fig. 10a), whilst $\delta^{13}C$ values show less variability and lie mainly between -8‰ and -10‰ (Fig. 10b), neither record showing any strong trend. Data from ODP976 show Mg/Ca SSTs oscillating between 14ºC and 18ºC (Fig. 11f), and *G. Bulloides* $\delta^{18}O$ fluctuating by ~0.5‰ between 132.0-130.5 ka superimposed on a strong negative trend starting at ~133.0 ka (Fig. 11h) (Jimenez-Amat and Zahn, 2015). The instability evident in the marine data may relate to cold water incursions into the Mediterranean from the Atlantic during H11 (Jimenez-Amat and Zahn, 2015). Variability of ~4ºC in SSTs would strongly influence regional rainfall amounts, the isotopic composition of which would initially be controlled by that of marine surface water. The presence of thin aragonite layers within the predominantly calcitic Dim 1 implies periodic increases in groundwater residence times and lower drip rates (Frisia and Borsato, 2010) and supports the isotopic evidence for periodic fluctuations in effective rainfall amounts at this time in the Eastern Mediterranean.

Between ~130.2 ka and ~129.4 ka on the Dim timescale, increases in $\delta^{18}O$ and $\delta^{13}C$ values of up to 0.9‰ and 3.5‰ respectively are associated with a shift in the growth axis and indicate a period of drier conditions which may be related to the ~4ºC temperature drop recorded in the marine Mg/Ca data at ~130.6 ka (Jimenez-Amat and Zahn, 2015), towards the end of H11 (Fig. 11f). Contemporaneous pollen records from Lake Van in eastern Turkey (Pickarski et al., 2015) demonstrate increasing abundance of *Pistacia* between 131.2-129.1 ka, indicating dry summer and mild winter conditions. After 129.4 ka, $\delta^{18}O$ and $\delta^{13}C$ values fall by 1.5‰ and 2.0‰ to -7.5‰ and -12‰ respectively, although these trends are erratic and brief positive excursions recur, especially in the $\delta^{18}O$ record at ~128.7 ka. The decreases in Dim 1 $\delta^{18}O$ and $\delta^{13}C$ coincide with strong $\delta^{18}O$ negative trends in Corchia Cave (Drysdale et al., 2009) and Soreq Cave speleothems (Bar-Matthews et al., 2003). Depletions of ~0.5‰ in *G. Bulloides* $\delta^{18}O$ (Jimenez-Amat and Zahn, 2015) (Fig. 11h) imply some influence from a marine moisture source, but nevertheless the Dim 1 oxygen and carbon data taken together indicate an increasingly wetter and more densely vegetated local environment. These changes correspond with the onset of the East Asian Monsoon (EAM) at the beginning of the LIG which is recorded at 129.0 ka in China by large abrupt negative $\delta^{18}O$ shifts in speleothems D4 from Dongge Cave (Kelly et al., 2006) (Fig. 11d) and SB25 from Sanbao Cave (Cheng et al., 2009a). However, the continued presence within this phase of transient positive stable isotope excursions in Dim 1 demonstrates that the brief drier intervals remained a characteristic of climate in the Eastern Mediterranean at this time.

At 130 ka -129 ka a general increase in extension rates occurs in speleothems Dim 1 (Fig. 8), Corchia CC5, and TCU D4, (Drysdale et al., 2009; Regattieri et al., 2014) and deposition of stalagmite K1 2010 commenced in Kaanan Cave, Lebanon (Nehme et al., 2015). Marine Mg/Ca and alkenone records imply rapid ~5^{0}C increases in SST at ~129 ka (Fig. 10f,g) (Jimenez-Amat and Zahn, 2015; Marino et al., 2015) which may have stimulated significant increases in Mediterranean rainfall, narrowly predating the onset of sapropel S5 at ~128.3 ka (Grant et al., 2016). The wetter phase at Dim Cave persisted for several hundred years until ~128.6 ka when $\delta^{18}O$ and $\delta^{13}C$ values increase rapidly but irregularly to -5.3‰ and -3.5‰

respectively (Fig. 10a,b), implying strong reductions in groundwater recharge and soil productivity. Such elevated $\delta^{13}C$ values and the switch from calcite to aragonite during maximum oxygen and carbon isotope enrichment indicate increases in PCP and Mg/Ca ratios as a consequence of longer groundwater contact time within dolomitic bedrock. Aragonite deposition was rare in Dim Cave through the last glacial-interglacial cycle but did occur between 80-75 ka, at which time $\delta^{18}O$ and $\delta^{13}C$ values peak at -3.5‰ and -5.0‰ respectively (Unal-Imer et al., 2015; Ünal-Imer et al., 2016), comparable to those recorded in the aragonite of Dim 1.

$^{87}Sr/^{86}Sr$ values experienced a two-phase decrease, separated by a slight recovery, at ~128.7 ka. The initial fall coincides with the negative trends in $\delta^{13}C$ and $\delta^{18}O$ signifying increasing precipitation, and the second with the strong positive stable isotope excursions and change to aragonite deposition, indicative of drier conditions (Fig. 10c). The first phase may be analogous to the significant drop in Sr isotope values seen in marine core ODP 658C at ~12.5 ka following a reduction in the dust supply as the African Monsoon strengthened at the beginning of the Holocene African Humid Period, (Cole et al., 2009). The expansion of vegetation across North Africa at the beginning of the LIG following intensification of the Asian and African Monsoon circulations at 129 ka would similarly have reduced long range aeolian dust transport at this time. Alternatively, lower $^{87}Sr/^{86}Sr$ ratios may derive from increased groundwater infiltration and intensified leaching within the epikarst, although this might be partially counteracted by simultaneous release of more radiogenic Sr from the soil zone (Fig. 7). The second phase of $^{87}Sr/^{86}Sr$ decrease, during the period of oxygen and carbon isotopic enrichment, is compatible with increased groundwater residence times and consequent increase in water-bedrock interaction following substantial reductions in annual recharge.

Some regional pollen data also contain evidence of a drier phase at ~128 ka, although chronologies for these records are less secure (Govin et al., 2015; Zanchetta et al., 2016). At Lago Grande di Monticchio (LGdM), in southern Italy, arboreal pollen abundances decrease between 128.15 ka and 127.90 ka (Allen and Huntley, 2009; Brauer et al., 2007), and a brief (decadal to century-scale) reduction in temperate tree pollen occurs at Tenaghi Phillipon (TP), northeast Greece, at ~128.4 ka just prior to arboreal-dominated taxa reaching fully interglacial abundances (Milner et al., 2012). However, no equivalent event is seen at Ioannina, northwest Greece (Tzedakis et al., 2003). Marine core MD95-2042 on the Iberian Margin (Sanchez Goni et al., 1999) records peak abundance of warm humid-temperate pollen occurring early in the LIG, preceded by a "Younger Dryas-like event". The precise date of this event is uncertain, but it probably lies between 128 ka and 129 ka (Govin et al., 2015) and may correlate with the transient declines in arboreal pollen at LGdM and TP. A decline in temperate tree pollen is also recorded at this time in core MD01-2444 from the Portuguese Margin where it is correlated with cold water event 28 (C28) at ~128.7 ka (Tzedakis et al., 2018).

The oxygen, carbon and strontium isotope excursion peaks in Dim 1 are immediately followed by the prominent hiatus, which occurs as the isotopic indicators signal increasing moisture availability (Fig. 6). The break in growth may denote a second, more severe, phase of rainfall reduction which caused growth to stop, following which renewed heavy rainfall and rapid infiltration of under-saturated groundwaters eroded the stalagmite cap. Alternatively, carbonate erosion may have occurred, without prior cessation of growth, due to a sudden intensification of rainfall which substantially increased flow rate through the epikarst, and forced under-saturated, aggressive, seepage water into the cave. In either case, the brief time-interval represented by non-deposition (see below) suggests complete or partial removal of ~1-3 mm of aragonite in the axial zone. Above the hiatus, calcite deposition recommenced along an offset axis, with strong negative trends in both $\delta^{18}O$ and $\delta^{13}C$ reaching minimum values of -7.8‰ and -13.8‰ respectively at ~128.5 ka. These are 1-2‰ more negative than early Holocene values (Unal-Imer et al., 2015), implying wetter conditions and well-developed soil and dense vegetation cover above the cave at that time. $^{87}Sr/^{86}Sr$ ratios also reach values similar to, or slightly higher, than before the dry phase, probably due to an increased soil contribution. Stable isotope data from LIG speleothems generally show that minimum values, indicating maximum moisture availability, are attained at ~128 ka, at the beginning of the interglacial. In the Mediterranean this pattern is seen in Corchia Cave (Drysdale et al., 2009) and Soreq Cave (Bar-Matthews et al., 2003), and also in China, at Dongge Cave (Kelly et al., 2006). The Dim 1 stable isotope data broadly form the same pattern as seen in other contemporary speleothems, but appear to reach minimum values ~0.6 ka before those in other speleothems (Fig. 11a-e). It is highly unlikely that the geochemical signals in this speleothem could be out of phase with those in all other speleothems across the region and it is probable that the age model over-estimates ages towards the top of Dim 1 by a few hundred years. Detailed comparison of $\delta^{18}O$ structure through the positive excursion with speleothem data from France and Austria (Section 5.5) supports this interpretation. Subsequent increases of about 1‰ and 1.5‰ in $\delta^{18}O$ and $\delta^{13}C$ respectively, trends widely seen in other contemporary speleothems (Fig. 11c-e), are likely to document reducing precipitation.

5.5. Nature and origin of the positive isotopic anomaly

The rapid increases in $\delta^{18}O$ and $\delta^{13}C$ values and abrupt fall in $^{87}Sr/^{86}Sr$ between 128 ka and 129 ka, culminating in a switch from calcite to alternating aragonite-calcite precipitation, clearly record a major environmental change in Dim Cave. A change from calcite to aragonite mineralogy in a speleothem is generally a strong indicator of reducing effective rainfall (Railsback et al., 1994; Wassenburg et al., 2012) and the isotopic evidence supports this interpretation. The large amplitude of the $\delta^{18}O$ anomaly (~2.0‰) is similar to that reported from Soreq Cave for the Younger Dryas (YD) (Bar-Matthews et al., 2003) and to the shift from YD to early Holocene values in speleothem Dim-E2 (Fig. S7) (Unal-Imer et al., 2015). However, the two events differ significantly in duration and also because YD speleothem $\delta^{18}O$ signals incorporate strong moisture source and temperature effects deriving from complex atmosphere-ocean changes associated with deglaciation (Baldini et al., 2015). Nevertheless, a marked increase in aridity across Eurasia during the YD is widely recognised (Belli et al., 2017; Brauer et al., 2008; Rach et al., 2014; Wang et al., 2001), although the presence of drier conditions in the Eastern Mediterranean at that time is debated (Hartman et al., 2016), and the Dim 1 and YD events may, therefore, have a similar origin, namely a cooling of the North Atlantic and slowdown of the MOC (Ritz et al., 2013), the impacts of which were most evident in winter.

Early LIG $\delta^{18}O$ enrichment episodes also occur in European speleothems, most prominently in BD Cave in southwest France (Couchoud et al., 2009) and Schneckenloch Cave, Austria (Moseley et al., 2015) where stalagmites BD-Inf and SCH-5 record increases of 0.85‰ and 1.60‰ respectively in $\delta^{18}O$ values between 128.4 ka and 128.0 ka (Fig. 12). Within the 2 s.d. dating errors, these are compatible with the ~128.6 ka age of the positive $\delta^{18}O$ and $\delta^{13}C$ peaks in Dim 1 and there are strong similarities in the structures of these isotopic events which suggest that they probably have a common origin. Consequently, it is unlikely that the isotopic and petrographic shifts seen in Dim 1 can be attributed to cave-specific factors. Transferring this part of the $\delta^{18}O$ record to the more robust BD timescale (Fig. 12) using prominent isotopic features as tie points (Fig. S8), the ~100 year timespan of the main positive peak in BD Cave provides an estimate of about 20 years for the missing aragonite deposition represented by the Dim 1 hiatus. The equivalent phase of the Schneckenloch Cave event also lasted about 100 years (Fig. 12). Since the hiatus in Dim 1 occurs during the negative-trending limb of the excursion and neither BD-Inf nor SCH-5 show a reversal of that trend in the equivalent location, it is unlikely that growth in Dim 1 ceased due to drip-water starvation prior to carbonate corrosion. Whilst the Dim and BD oxygen isotope signals are interpreted as recording fluctuations in rainfall amounts, the Schneckenloch data are considered primarily to record changes in local atmospheric temperature (Moseley et al., 2015). Evidently the Northern Alps experienced a warming event at a time of reduced rainfall on the Atlantic seaboard and in the Eastern Mediterranean, possibly due to northward advection of warm Mediterranean air carrying isotopically enriched water vapour during a temporary weakening of the zonal westerly flow. Alternatively, the positive $\delta^{18}O$ anomaly might represent a change in rainfall seasonality from a winter to a summer maximum, perhaps as a consequence of reduced winter cyclogenesis.

The identification of a cool dry phase in southwest France (Couchoud et al., 2009), coeval within error with the Dim 1 isotopic enrichment event, suggests that the origin of that event lies in the North Atlantic rather than within the Mediterranean. Variations in North Atlantic ocean circulation, particularly the MOC, are strongly linked to SSTs which in turn influence moisture supply downstream over Eurasia. Speleothem stable isotope data from the Eastern Mediterranean document abrupt changes in precipitation amounts through the last glacial period related to variations in sea ice cover and SSTs in the North Atlantic (Bar-Matthews et al., 2003; Drysdale et al., 2009; Rowe et al., 2012; Unal-Imer et al., 2015). A 3ºC SST drop occurs in the ODP976 Mg/Ca record at ~128.3 ka (Fig. 11f) which has been likened to a Younger Dryas-type event (Jimenez-Amat and Zahn, 2015), although a similar drop is not seen in the alkenone record and Mediterranean SSTs remained well above values recorded between 132 ka - 129 ka during which time Dim 1 was mainly precipitating calcite. The Mg/Ca data may, however, represent an attenuated signal from a larger North Atlantic event. A recent study (Tzedakis et al., 2018) has attempted to correlate positive U/Th-dated $\delta^{18}O$ excursions in Corchia Cave speleothem with reductions in arboreal pollen abundance in marine core MD01-2444 from the Portuguese Margin and subsequently to correlate the stratigraphy of that core with others from the North Atlantic containing evidence of cold water incursions (Galaasen et al., 2014; Mokeddem et al., 2014; Nicholl et al., 2012). A strong association is found between North Atlantic cooling, disruption of the MOC and arid phases in the Mediterranean as manifested by reduced tree pollen abundances and positive $\delta^{18}O$ shifts in the Corchia Cave speleothem records. One such cold water incursion (C28) with a duration of ~300 years is identified at ~128.7 ka, close to the ages assigned to the Dim, BD and Schneckenloch Cave isotopic enrichments. This event provides a potential forcing mechanism for modifying the mid-latitude westerly circulation pattern and inducing winter rainfall reductions across Northwest Europe and the Mediterranean.

The duration and structure of the Dim event are strikingly similar to the well documented Holocene 8.2 ka event recorded in Greenland ice cores (Fig. S9) and in speleothems from China, Brazil and Oman (Cheng et al., 2009b), although rather muted in Mediterranean records. That event may have resulted from an outburst flood from glacial Lake Agassiz into the Labrador Sea, or from the collapse of the Hudson Bay ice saddle (Matero et al., 2017), which temporarily disrupted the North Atlantic MOC, the impact of which persisted in the isotope records for ~200-300 years (Cheng et al., 2009b). The origin of the C28 event is not known but is presumably related to high latitude ice melting, and in this context the poly-phase isotope pattern and duration are interesting as it occurs near the beginning of the LIG rather than towards the middle, as in the Holocene. There appears to be less evidence for widespread global cooling early in the LIG compared to that available for the Holocene 8.2 ka event, which may reflect an absence of persistent or extensive NA winter sea ice during the particularly warm LIG (Galaasen et al., 2014). Sea ice effectively suppresses winter cyclogenesis and has a strong cooling effect downstream as illustrated by weaker Asian Monsoon circulation during glacial periods and Heinrich Stadial Events, but colder SSTs in the absence of sea ice have much less impact on atmospheric circulation patterns. The speleothem evidence is compatible with a cold but largely ice-free North Atlantic leading to winter rainfall reductions in NW Europe and the Mediterranean.

6. Conclusions

Stable isotope records from stalagmite Dim 1, which grew through the latter part of TII between ~132 ka and ~128 ka, reflect a combination of changes in marine boundary conditions and increases in precipitation as the hydrological cycle strengthened in response to rising global temperatures. Strongly negative $\delta^{18}O$ values indicate that the onset of the LIG in southern Turkey was wetter than the early Holocene, supporting previous evidence from contemporary Mediterranean stalagmites. Speleothem growth in Dim Cave appears particularly sensitive to fluctuations in seasonal groundwater recharge and episodes of aragonite deposition and subsequent partial removal by under-saturated drip waters show that there were frequent brief drier cycles followed by rapid infiltration of renewed heavy rainfall.

A phase of strong oxygen and carbon isotope enrichment and lower Sr isotope values, lasting for 200-300 years and centred around 128.1 ka, incorporates a switch from calcite to alternating aragonite/calcite deposition, demonstrating a more severe and prolonged reduction in (winter) precipitation. Rainfall amounts fell from significantly above to rather below present day totals. This drier phase is succeeded by the wettest conditions in the record, signified by minimum $\delta^{18}O$ and $\delta^{13}C$ values, causing rapid groundwater infiltration and corrosion of the stalagmite upper surface.

The dating and structure of the positive isotopic anomaly suggest that it correlates with positive oxygen isotope peaks in stalagmites from Bourgeois-Delaunay Cave, southwest France and Schneckenloch Cave, Austria. These peaks are probably associated with cold water event C28 in the North Atlantic and their poly-phase isotopic structures strongly resemble Northern Hemisphere speleothem $\delta^{18}O$ records of the Holocene 8.2 ka event which was also caused by an outburst of glacial freshwater into the North Atlantic. The ~128 ka event it is not widely recognised in terrestrial archives within the Mediterranean Basin or globally, possibly because the temporal resolution of many climate records is inadequate to capture such a brief episode.

Acknowledgements

We thank cave owner Fuat Şaroğlu, and manager Murat Ünal for their permission to sample speleothem and for help and support during this project; we also thank Bertrand Leze for assistance with optical and scanning electron microscope instrumentation. Letty Wickens acknowledges receipt of NERC studentship grant NE/G524101/1, and Emily Peckover receipt of a NERC studentship through grants NE/L50158X/1 & NE/K500896/1. Support for

U/Th dating was through award IP-1410-1110 from the NERC Isotope Geosciences Facility. We are grateful to Professor R. Parrish and staff members of the Facility for valuable discussions through the course of this project. The manuscript was greatly improved by the comments of two anonymous referees.

Appendix A. Datasets and Supplementary Information

Supplementary data for this article can be found online at:

References

Allen, J. R. M., Brandt, U., Brauer, A., Hubberten, H. W., Huntley, B., Keller, J., Kraml, M., Mackensen, A., Mingram, J., Negendank, J. F. W., Nowaczyk, N. R., Oberhänsli, H., Watts, W. A., Wulf, S., and Zolitschka, B., 1999, Rapid environmental changes in southern Europe during the last glacial period: Nature, v. 400, no. 6746, p. 740-743.

Allen, J. R. M., and Huntley, B., 2009, Last Interglacial palaeovegetation, palaeoenvironments and chronology: a new record from Lago Grande di Monticchio, southern Italy: Quaternary Science Reviews, v. 28, no. 15-16, p. 1521-1538.

Alpert, P., Neeman, B. U., and Shay-El, Y., 1990, Climatological analysis of Mediterranean cyclones using ECMWF data: Tellus, Series A, v. 42 A, no. 1, p. 65-77.

Andersen, K. K., Azuma, N., Barnola, J. M., Bigler, M., Biscaye, P., Caillon, N., Chappellaz, J., Clausen, H. B., Dahl-Jensen, D., Fischer, H., Flückiger, J., Fritzsche, D., Fujii, Y., Goto-Azuma, K., Grønvold, K., Gundestrup, N. S., Hansson, M., Huber, C., Hvidberg, C. S., Johnsen, S. J., Jonsell, U., Jouzel, J., Kipfstuhl, S., Landais, A., Leuenberger, M., Lorrain, R., Masson-Delmotte, V., Miller, H., Motoyama, H., Narita, H., Popp, T., Rasmussen, S. O., Raynaud, D., Rothlisberger, R., Ruth, U., Samyn, D., Schwander, J., Shoji, H., Siggard-Andersen, M. L., Steffensen, J. P., Stocker, T., Sveinbjörnsdóttir, A. E., Svensson, A., Takata, M., Tison, J. L., Thorsteinsson, T., Watanabe, O., Wilhelms, F., and White, J. W. C., 2004, High-resolution record of Northern Hemisphere climate extending into the last interglacial period: Nature, v. 431, no. 7005, p. 147-151.

Bajo, P., Hellstrom, J., Frisia, S., Drysdale, R., Black, J., Woodhead, J., Borsato, A., Zanchetta, G., Wallace, M. W., Regattieri, E., and Haese, R., 2016, "Cryptic" diagenesis and its implications for speleothem geochronologies: Quaternary Science Reviews, v. 148, p. 17-28.

Baker, R. G., Bettis, E. A., Denniston, R. F., Gonzalez, L. A., Strickland, L. E., and Krieg, J. R., 2002, Holocene paleoenvironments in southeastern Minnesota - Chasing the prairie-forest ecotone: Palaeogeography, Palaeoclimatology, Palaeoecology, v. 177, no. 1-2, p. 103-122.

Baldini, L. M., McDermott, F., Baldini, J. U. L., Arias, P., Cueto, M., Fairchild, I. J., Hoffmann, D. L., Mattey, D. P., Müller, W., Nita, D. C., Ontañón, R., Garciá-Moncó, C., and Richards, D. A., 2015, Regional temperature, atmospheric circulation, and sea-ice variability within the Younger Dryas Event constrained using a speleothem from northern Iberia: Earth and Planetary Science Letters, v. 419, p. 101-110.

Bar-Matthews, M., Ayalon, A., Gilmour, M., Matthews, A., and Hawkesworth, C. J., 2003, Sea-land oxygen isotopic relationships from planktonic foraminifera and speleothems in the Eastern Mediterranean region and their implication for paleorainfall during interglacial intervals: Geochimica et Cosmochimica Acta, v. 67, no. 17, p. 3181-3199.

Bar-Matthews, M., Ayalon, A., and Kaufman, A., 1997, Late Quaternary Paleoclimate in the Eastern Mediterranean Region from Stable Isotope Analysis of Speleothems at Soreq Cave, Israel: Quaternary Research, v. 47, no. 2, p. 155-168.

Bard, E., Delaygue, G., Rostek, F., Antonioli, F., Silenzi, S., and Schrag, D. P., 2002, Hydrological conditions over the western Mediterranean basin during the deposition of the cold Sapropel 6 (ca. 175 Kyr BP): Earth and Planetary Science Letters, v. 202, no. 2, p. 481-494.

Baykara, M. O., 2014, Güneybatı Anadolu’da mağara çökellerinin incelenmesi ve paleoiklimsel değerlendirmeleri. Doctoral dissertation, Pamukkale Üniversitesi Fen Bilimleri Enstitüsü].

Belli, R., Borsato, A., Frisia, S., Drysdale, R., Maas, R., and Greig, A., 2017, Investigating the hydrological significance of stalagmite geochemistry (Mg, Sr) using Sr isotope and particulate element records across the Late Glacial-to-Holocene transition: Geochimica et Cosmochimica Acta, v. 199, p. 247-263.

Bosmans, J. H. C., Drijfhout, S. S., Tuenter, E., Hilgen, F. J., Lourens, L. J., and Rohling, E. J., 2015, Precession and obliquity forcing of the freshwater budget over the Mediterranean: Quaternary Science Reviews, v. 123, p. 16-30.

Bottema, S., 1995, The Younger Dryas in the Eastern Mediterranean: Quaternary Science Reviews, v. 14, no. 9, p. 883-891.

Bozkurt, D., and Sen, O. L., 2011, Precipitation in the Anatolian Peninsula: Sensitivity to increased SSTs in the surrounding seas: Climate Dynamics, v. 36, no. 3, p. 711-726.

Brauer, A., Allen, J. R. M., Mingram, J., Dulski, P., Wulf, S., and Huntley, B., 2007, Evidence for last interglacial chronology and environmental change from Southern Europe: Proceedings of the National Academy of Sciences of the United States of America, v. 104, no. 2, p. 450-455.

Brauer, A., Haug, G. H., Dulski, P., Sigman, D. M., and Negendank, J. F. W., 2008, An abrupt wind shift in western Europe at the onset of the Younger Dryas cold period: Nature Geoscience, v. 1, no. 8, p. 520-523.

Cheng, H., Edwards, R. L., Broecker, W. S., Denton, G. H., Kong, X. G., Wang, Y. J., Zhang, R., and Wang, X. F., 2009a, Ice Age Terminations: Science, v. 326, no. 5950, p. 248-252.

Cheng, H., Fleitmann, D., Edwards, R. L., Wang, X., Cruz, F. W., Auler, A. S., Mangini, A., Wang, Y., Kong, X., Burns, S. J., and Matter, A., 2009b, Timing and structure of the 8.2. kyr B.P. event inferred from $\delta^{18}O$ records of stalagmites from China, Oman, and Brazil: Geology, v. 37, no. 11, p. 1007-1010.

Cole, J. M., Goldstein, S. L., deMenocal, P. B., Hemming, S. R., and Grousset, F. E., 2009, Contrasting compositions of Saharan dust in the eastern Atlantic Ocean during the last deglaciation and African Humid Period: Earth and Planetary Science Letters, v. 278, no. 3-4, p. 257-266.

Coope, G. R., and Lemdahl, G., 1995, Regional differences in the Lateglacial climate of northern Europe based on coleopteran analysis: Journal of Quaternary Science, v. 10, no. 4, p. 391-395.

Coope, G. R., Lemdahl, G., Lowe, J. J., and Walkling, A., 1998, Temperature gradients in northern Europe during the last glacial-Holocene transition (14-9 14C kyr BP) interpreted from coleopteran assemblages: Journal of Quaternary Science, v. 13, no. 5, p. 419-433.

Coplen, T. B., 2007, Calibration of the calcite-water oxygen-isotope geothermometer at Devils Hole, Nevada, a natural laboratory: Geochimica et Cosmochimica Acta, v. 71, no. 16, p. 3948-3957.

Couchoud, I., Genty, D., Hoffmann, D., Drysdale, R., and Blamart, D., 2009, Millennial-scale climate variability during the Last Interglacial recorded in a speleothem from south-western France: Quaternary Science Reviews, v. 28, no. 27-28, p. 3263-3274.

Daley, T. J., Thomas, E. R., Holmes, J. A., Street-Perrott, F. A., Chapman, M. R., Tindall, J. C., Valdes, P. J., Loader, N. J., Marshall, J. D., Wolff, E. W., Hopley, P. J., Atkinson, T., Barber, K. E., Fisher, E. H., Robertson, I., Hughes, P. D. M., and Roberts, C. N., 2011, The 8200 yr BP cold event in stable isotope records from the North Atlantic region: Global and Planetary Change, v. 79, no. 3-4, p. 288-302.

Dansgaard, W., 1964, Stable Isotopes in Precipitation: Tellus, Series A, v. 16, p. 436-468.

De Choudens-Sánchez, V., and Gonzalez, L. A., 2009, Calcite and aragonite precipitation under controlled instantaneous supersaturation: Elucidating the role of CACO <inf>3</inf> saturation state and Mg/Ca ratio on calcium carbonate polymorphism: Journal of Sedimentary Research, v. 79, no. 6, p. 363-376.

Dietzel, M., Tang, J., Leis, A., and Köhler, S. J., 2009, Oxygen isotopic fractionation during inorganic calcite precipitation - Effects of temperature, precipitation rate and pH: Chemical Geology, v. 268, no. 1-2, p. 107-115.

Dirican, A., Ünal, S., Acar, Y., and Demircan, M., 2005, The temporal and seasonal variation of H-2 and O-18 in atmospheric water vapour and precipitation from Ankara, Turkey in relation to air mass trajectories at Mediterranean Basin, Isotopic Composition of Precipitation in the Mediterranean Basin in Relation to Air Circulation Patterns and Climate, Volume 191, IAEA.

Domínguez-Villar, D., Krklec, K., Pelicon, P., Fairchild, I. J., Cheng, H., and Edwards, L. R., 2017, Geochemistry of speleothems affected by aragonite to calcite recrystallization – Potential inheritance from the precursor mineral: Geochimica et Cosmochimica Acta, v. 200, p. 310-329.

Dorale, J. A., González, L. A., Reagan, M. K., Pickett, D. A., Murrell, M. T., and Baker, R. G., 1992, A high-resolution record of holocene climate change in speleothem calcite from Cold Water Cave, Northeast Iowa: Science, v. 258, no. 5088, p. 1626-1630.

Dorale, J. A., and Liu, Z., 2009, Limitations of hendy test criteria in judging the paleoclimatic suitability of speleothems and the need for replication: Journal of Cave and Karst Studies, v. 71, no. 1, p. 73-80.

Drysdale, R. N., Hellstrom, J. C., Zanchetta, G., Fallick, A. E., Goni, M. F. S., Couchoud, I., McDonald, J., Maas, R., Lohmann, G., and Isola, I., 2009, Evidence for obliquity forcing of glacial termination II: Science, v. 325, no. 5947, p. 1527-1531.

Fairchild, I. J., Borsato, A., Tooth, A. F., Frisia, S., Hawkesworth, C. J., Huang, Y., McDermott, F., and Spiro, B., 2000, Controls on trace element (Sr-Mg) compositions of carbonate cave waters: Implications for speleothem climatic records: Chemical Geology, v. 166, no. 3-4, p. 255-269.

Fairchild, I. J., Smith, C. L., Baker, A., Fuller, L., Spötl, C., Mattey, D., and McDermott, F., 2006, Modification and preservation of environmental signals in speleothems: Earth-Science Reviews, v. 75, no. 1-4, p. 105-153.

Fohlmeister, J., Arps, J., Spötl, C., Schröder-Ritzrau, A., Plessen, B., Günter, C., Frank, N., and Trüssel, M., 2018, Carbon and oxygen isotope fractionation in the water-calcite-aragonite system: Geochimica et Cosmochimica Acta, v. 235, p. 127-139.

Frisia, S., 2015, Microstratigraphic logging of calcite fabrics in speleothems as tool for palaeoclimate studies: International Journal of Speleology, v. 44, no. 1, p. 1-16.

Frisia, S., and Borsato, A., 2010, Chapter 6 Karst, Developments in Sedimentology, Volume 61, p. 269-318.

Frisia, S., Borsato, A., Fairchild, I. J., McDermott, F., and Selmo, E. M., 2002, Aragonite-calcite relationships in speleothems (Grotte de Clamouse, France): Environment, fabrics, and carbonate geochemistry: Journal of Sedimentary Research, v. 72, no. 5, p. 687-699.

Frisia, S., Fairchild, I. J., Fohlmeister, J., Miorandi, R., Spötl, C., and Borsato, A., 2011, Carbon mass-balance modelling and carbon isotope exchange processes in dynamic caves: Geochimica et Cosmochimica Acta, v. 75, no. 2, p. 380-400.

Galaasen, E. V., Ninnemann, U. S., Irvali, N., Kleiven, H. F., Rosenthal, Y., Kissel, C., and Hodell, D. A., 2014, Rapid reductions in North Atlantic Deep Water during the peak of the last interglacial period: Science, v. 343, no. 6175, p. 1129-1132.

Genty, D., Blamart, D., Ouahdi, R., Gilmour, M., Baker, A., Jouzel, J., and Van-Exter, S., 2003, Precise dating of Dansgaard-Oeschger climate oscillations in western Europe from stalagmite data: Nature, v. 421, no. 6925, p. 833-837.

Gonzalez, L. A., Carpenter, S. J., and Lohmann, K. C., 1992, Inorganic calcite morphology: roles of fluid chemistry and fluid flow: Journal of Sedimentary Petrology, v. 62, no. 3, p. 382-399.

Govin, A., Capron, E., Tzedakis, P. C., Verheyden, S., Ghaleb, B., Hillaire-Marcel, C., St-Onge, G., Stoner, J. S., Bassinot, F., Bazin, L., Blunier, T., Combourieu-Nebout, N., El Ouahabi, A., Genty, D., Gersonde, R., Jimenez-Amat, P., Landais, A., Martrat, B., Masson-Delmotte, V., Parrenin, F., Seidenkrantz, M. S., Veres, D., Waelbroeck, C., and Zahn, R., 2015, Sequence of events from the onset to the demise of the Last Interglacial: Evaluating strengths and limitations of chronologies used in climatic archives: Quaternary Science Reviews, v. 129, p. 1-36.

Grant, K. M., Grimm, R., Mikolajewicz, U., Marino, G., Ziegler, M., and Rohling, E. J., 2016, The timing of Mediterranean sapropel deposition relative to insolation, sea-level and African monsoon changes: Quaternary Science Reviews, v. 140, p. 125-141.

Grant, K. M., Rohling, E. J., Bar-Matthews, M., Ayalon, A., Medina-Elizalde, M., Ramsey, C. B., Satow, C., and Roberts, A. P., 2012, Rapid coupling between ice volume and polar temperature over the past 50,000 years: Nature, v. 491, no. 7426, p. 744-747.

Grossman, E. L., and Ku, T. L., 1986, Oxygen and carbon isotope fractionation in biogenic aragonite: Temperature effects: Chemical Geology, v. 59, no. 1, p. 59-74.

Hartman, G., Bar-Yosef, O., Brittingham, A., Grosman, L., and Munro, N. D., 2016, Hunted gazelles evidence cooling, but not drying, during the Younger Dryas in the southern Levant: Proceedings of the National Academy of Sciences of the United States of America, v. 113, no. 15, p. 3997-4002.

Hendy, C. H., 1971, The isotopic geochemistry of speleothems-I. The calculation of the effects of different modes of formation on the isotopic composition of speleothems and their applicability as palaeoclimatic indicators: Geochimica et Cosmochimica Acta, v. 35, no. 8, p. 801-824.

Holmgren, K., Lee-Thorp, J. A., Cooper, G. R. J., Lundblad, K., Partridge, T. C., Scott, L., Sithaldeen, R., Talma, A. S., and Tyson, P. D., 2003, Persistent millennial-scale climatic variability over the past 25,000 years in Southern Africa: Quaternary Science Reviews, v. 22, no. 21-22, p. 2311-2326.

IAEA/WMO, Global Network of Isotopes in Precipitation., The GNIP Database Volume 2015.

Irvali, N., Ninnemann, U. S., Galaasen, E. V., Rosenthal, Y., Kroon, D., Oppo, D. W., Kleiven, H. F., Darling, K. F., and Kissel, C., 2012, Rapid switches in subpolar North Atlantic hydrography and climate during the Last Interglacial (MIS 5e): Paleoceanography, v. 27, no. 2.

Jimenez-Amat, P., and Zahn, R., 2015, Offset timing of climate oscillations during the last two glacial-interglacial transitions connected with large-scale freshwater perturbation: Paleoceanography, v. 30, no. 6, p. 768-788.

Kandiano, E. S., Bauch, H. A., and Fahl, K., 2014, Last interglacial surface water structure in the western Mediterranean (Balearic) Sea: Climatic variability and link between low and high latitudes: Global and Planetary Change, v. 123, p. 67-76.

Karaca, M., Deniz, A., and Tayanc, M., 2000, Cyclone track variability over Turkey in association with regional climate: International Journal of Climatology, v. 20, no. 10, p. 1225-1236.

Kaspar, F., Spangehl, T., and Cubasch, U., 2007, Northern hemisphere winter storm tracks of the Eemian interglacial and the last glacial inception: Climate of the Past, v. 3, no. 2, p. 181-192.

Kaufman, A., Wasserburg, G. J., Porcelli, D., Bar-Matthews, M., Ayalon, A., and Halicz, L., 1998, U-Th isotope systematics from the Soreq cave, Israel and climatic correlations: Earth and Planetary Science Letters, v. 156, no. 3-4, p. 141-155.

Kelly, M. J., Edwards, R. L., Cheng, H., Yuan, D., Cai, Y., Zhang, M., Lin, Y., and An, Z., 2006, High resolution characterization of the Asian Monsoon between 146,000 and 99,000 years B.P. from Dongge Cave, China and global correlation of events surrounding Termination II: Palaeogeography, Palaeoclimatology, Palaeoecology, v. 236, no. 1-2, p. 20-38.

Kendall, A. C., and Broughton, P. L., 1978, Origin of fabrics in speleothems composed of columnar calcite crystals: Journal of Sedimentary Petrology, v. 48, no. 2, p. 519-538.

Kim, S. T., and O'Neil, J. R., 1997, Equilibrium and nonequilibrium oxygen isotope effects in synthetic carbonates: Geochimica et Cosmochimica Acta, v. 61, no. 16, p. 3461-3475.

Kim, S. T., O'Neil, J. R., Hillaire-Marcel, C., and Mucci, A., 2007, Oxygen isotope fractionation between synthetic aragonite and water: Influence of temperature and Mg2+ concentration: Geochimica et Cosmochimica Acta, v. 71, no. 19, p. 4704-4715.

Krichak, S. O., and Alpert, P., 2005, Signatures of the NAO in the atmospheric circulation during wet winter months over the Mediterranean region: Theoretical and Applied Climatology, v. 82, no. 1-2, p. 27-39.

Kurt, L., Ketenoğlu, A. O., Akman, Y., Özdeniz, E., Şekerciler, F., Bölükbaşi, A., and Özbey, B. G., 2015, Syntaxonomic analysis of the preforest and forest vegetation in the thermo-and eumediterranean zone around Antalya Gulf, Turkey: Turkish Journal of Botany, v. 39, no. 3, p. 487-498.

Kutiel, H., and Benaroch, Y., 2002, North Sea-Caspian Pattern (NCP) - an upper level atmospheric teleconnection affecting the Eastern Mediterranean: Identification and definition: Theoretical and Applied Climatology, v. 71, no. 1-2, p. 17-28.

Kutiel, H., Maheras, P., Turkes, M., and Paz, S., 2002, North Sea Caspian Pattern (NCP) - an upper level atmospheric teleconnection affecting the eastern Mediterranean - implications on the regional climate: Theoretical and Applied Climatology, v. 72, no. 3-4, p. 173-192.

Kutzbach, J. E., Chen, G., Cheng, H., Edwards, R. L., and Liu, Z., 2014, Potential role of winter rainfall in explaining increased moisture in the Mediterranean and Middle East during periods of maximum orbitally-forced insolation seasonality: Climate Dynamics, v. 42, no. 3-4, p. 1079-1095.

Lachniet, M. S., 2009, Climatic and environmental controls on speleothem oxygen-isotope values: Quaternary Science Reviews, v. 28, no. 5-6, p. 412-432.

Lachniet, M. S., 2015, Are aragonite stalagmites reliable paleoclimate proxies? Tests for oxygen isotope time-series replication and equilibrium: Bulletin of the Geological Society of America, v. 127, no. 11-12, p. 1521-1533.

Lotter, A. F., Birks, H. J. B., Eicher, U., Hofmann, W., Schwander, J., and Wick, L., 2000, Younger Dryas and Allerod summer temperatures at Gerzensee (Switzerland) inferred from fossil pollen and cladoceran assemblages: Palaeogeography, Palaeoclimatology, Palaeoecology, v. 159, no. 3-4, p. 349-361.

Lowe, J. J., Rasmussen, S. O., Björck, S., Hoek, W. Z., Steffensen, J. P., Walker, M. J. C., and Yu, Z. C., 2008, Synchronisation of palaeoenvironmental events in the North Atlantic region during the Last Termination: a revised protocol recommended by the INTIMATE group: Quaternary Science Reviews, v. 27, no. 1-2, p. 6-17.

Marino, G., Rohling, E. J., Rodriguez-Sanz, L., Grant, K. M., Heslop, D., Roberts, A. P., Stanford, J. D., and Yu, J., 2015, Bipolar seesaw control on last interglacial sea level (vol 522, pg 197, 2015): Nature, v. 526, no. 7571.

Markowska, M., Baker, A., Treble, P. C., Andersen, M. S., Hankin, S., Jex, C. N., Tadros, C. V., and Roach, R., 2015, Unsaturated zone hydrology and cave drip discharge water response: Implications for speleothem paleoclimate record variability: Journal of Hydrology, v. 529, no. P2, p. 662-675.

Martín-García, R., Alonso-Zarza, A. M., Frisia, S., Rodríguez-Berriguete, Á., Drysdale, R., and Hellstrom, J., 2019, Effect of aragonite to calcite transformation on the geochemistry and dating accuracy of speleothems. An example from Castañar Cave, Spain: Sedimentary Geology, v. 383, p. 41-54.

Martrat, B., Grimalt, J. O., Lopez-Martinez, C., Cacho, I., Sierro, F. J., Flores, J. A., Zahn, R., Canals, M., Curtis, J. H., and Hodell, D. A., 2004, Abrupt temperature changes in the Western Mediterranean over the past 250,000 years: Science, v. 306, no. 5702, p. 1762-1765.

Martrat, B., Jimenez-Amat, P., Zahn, R., and Grimalt, J. O., 2014, Similarities and dissimilarities between the last two deglaciations and interglaciations in the North Atlantic region: Quaternary Science Reviews, v. 99, p. 122-134.

Matero, I. S. O., Gregoire, L. J., Ivanovic, R. F., Tindall, J. C., and Haywood, A. M., 2017, The 8.2 ka cooling event caused by Laurentide ice saddle collapse: Earth and Planetary Science Letters, v. 473, p. 205-214.

McDermott, F., 2004, Palaeo-climate reconstruction from stable isotope variations in speleothems: A review: Quaternary Science Reviews, v. 23, no. 7-8, p. 901-918.

McManus, J. F., Francois, R., Gherardl, J. M., Kelgwin, L., and Drown-Leger, S., 2004, Collapse and rapid resumption of Atlantic meridional circulation linked to deglacial climate changes: Nature, v. 428, no. 6985, p. 834-837.

McMillan, E. A., Fairchild, I. J., Frisia, S., Borsato, A., and McDermott, F., 2005, Annual trace element cycles in calcite-aragonite speleothems: Evidence of drought in the western Mediterranean 1200-1100 yr BP: Journal of Quaternary Science, v. 20, no. 5, p. 423-433.

Milner, A. M., Collier, R. E. L., Roucoux, K. H., Muller, U. C., Pross, J., Kalaitzidis, S., Christanis, K., and Tzedakis, P. C., 2012, Enhanced seasonality of precipitation in the Mediterranean during the early part of the Last Interglacial: Geology, v. 40, no. 10, p. 919-922.

Mokeddem, Z., McManus, J. F., and Oppo, D. W., 2014, Oceanographic dynamics and the end of the last interglacial in the subpolar North Atlantic: Proceedings of the National Academy of Sciences of the United States of America, v. 111, no. 31, p. 11263-11268.

Morse, J. W., and Mackenzie, F. T., 1990, Geochemistry of sedimentary carbonates: Geochemistry of sedimentary carbonates.

Moseley, G. E., Spötl, C., Cheng, H., Boch, R., Min, A., and Edwards, R. L., 2015, Termination-II interstadial/stadial climate change recorded in two stalagmites from the north European Alps: Quaternary Science Reviews, v. 127, p. 229-239.

Nehme, C., Verheyden, S., Noble, S. R., Farrant, A. R., Sahy, D., Hellstrom, J., Delannoy, J. J., and Claeys, P., 2015, Reconstruction of MIS 5 climate in the central Levant using a stalagmite from Kanaan Cave, Lebanon: Climate of the Past, v. 11, no. 12, p. 1785-1799.

Nicholl, J. A. L., Hodell, D. A., Naafs, B. D. A., Hillaire-Marcel, C., Channell, J. E. T., and Romero, O. E., 2012, A Laurentide outburst flooding event during the last interglacial period: Nature Geoscience, v. 5, no. 12, p. 901-904.

Okay, A. I., and Ozgul, N., 1984, HP/LT metamorphism and the structure of the Alanya Massif, Southern Turkey: An allochthonous composite tectonic sheet, Geological Society Special Publication, Volume 17, p. 429-439.

Ortega, R., Maire, R., Devès, G., and Quinif, Y., 2005, High-resolution mapping of uranium and other trace elements in recrystallized aragonite-calcite speleothems from caves in the Pyrenees (France): Implication for U-series dating: Earth and Planetary Science Letters, v. 237, no. 3-4, p. 911-923.

Osborne, A. H., Marino, G., Vance, D., and Rohling, E. J., 2010, Eastern Mediterranean surface water Nd during Eemian sapropel S5: monitoring northerly (mid-latitude) versus southerly (sub-tropical) freshwater contributions: Quaternary Science Reviews, v. 29, p. 2473-2483.

Peck, V. L., Hall, I. R., Zahn, R., and Elderfield, H., 2008, Millennial-scale surface and subsurface paleothermometry from the northeast Atlantic, 55-8 ka BP: Paleoceanography, v. 23, no. 3.

Pickarski, N., Kwiecien, O., Djamali, M., and Litt, T., 2015, Vegetation and environmental changes during the last interglacial in eastern Anatolia (Turkey): A new high-resolution pollen record from Lake Van: Palaeogeography, Palaeoclimatology, Palaeoecology, v. 435, p. 145-158.

Rach, O., Brauer, A., Wilkes, H., and Sachse, D., 2014, Delayed hydrological response to Greenland cooling at the onset of the Younger Dryas in western Europe: Nature Geoscience, v. 7, no. 2, p. 109-112.

Railsback, L. B., Brook, G. A., Jian, C., Kalin, R., and Fleisher, C. J., 1994, Environmental controls on the petrology of a late Holocene speleothem from Botswana with annual layers of aragonite and calcite: Journal of Sedimentary Research A: Sedimentary Petrology and Processes, v. 64 A, no. 1, p. 147-155.

Regattieri, E., Zanchetta, G., Drysdale, R. N., Isola, I., Hellstrom, J. C., and Roncioni, A., 2014, A continuous stable isotope record from the penultimate glacial maximum to the Last Interglacial (159-121ka) from Tana Che Urla Cave (Apuan Alps, central Italy): Quaternary Research (United States), v. 82, no. 2, p. 450-461.

Regattieri, E., Zanchetta, G., Drysdale, R. N., Isola, I., Woodhead, J. D., Hellstrom, J. C., Giaccio, B., Greig, A., Baneschi, I., and Dotsika, E., 2016, Environmental variability between the penultimate deglaciation and the mid Eemian: Insights from Tana che Urla (central Italy) speleothem trace element record: Quaternary Science Reviews, v. 152, p. 80-92.

Riechelmann, S., Schröder-Ritzrau, A., Wassenburg, J. A., Schreuer, J., Richter, D. K., Riechelmann, D. F. C., Terente, M., Constantin, S., Mangini, A., and Immenhauser, A., 2014, Physicochemical characteristics of drip waters: Influence on mineralogy and crystal morphology of recent cave carbonate precipitates: Geochimica et Cosmochimica Acta, v. 145, p. 13-29.

Ritz, S. P., Stocker, T. F., Grimalt, J. O., Menviel, L., and Timmermann, A., 2013, Estimated strength of the Atlantic overturning circulation during the last deglaciation: Nature Geoscience, v. 6, no. 3, p. 208-212.

Rohling, E. J., Marino, G., and Grant, K. M., 2015, Mediterranean climate and oceanography, and the periodic development of anoxic events (sapropels): Earth-Science Reviews, v. 143, p. 62-97.

Romanek, C. S., Grossman, E. L., and Morse, J. W., 1992, Carbon isotopic fractionation in synthetic aragonite and calcite: Effects of temperature and precipitation rate: Geochimica et Cosmochimica Acta, v. 56, no. 1, p. 419-430.

Rossi, C., and Lozano, R. P., 2016, Hydrochemical controls on aragonite versus calcite precipitation in cave dripwaters: Geochimica et Cosmochimica Acta, v. 192, p. 70-96.

Rowe, P. J., Mason, J. E., Andrews, J. E., Marca, A. D., Thomas, L., Van Calsteren, P., Jex, C. N., Vonhof, H. B., and Al-Omari, S., 2012, Speleothem isotopic evidence of winter rainfall variability in northeast Turkey between 77 and 6 ka: Quaternary Science Reviews, v. 45, p. 60-72.

Sanchez Goni, M. F., Eynaud, F., Turon, J. L., and Shackleton, N. J., 1999, High resolution palynological record off the Iberian margin: Direct land-sea correlation for the Last Interglacial complex: Earth and Planetary Science Letters, v. 171, no. 1, p. 123-137.

Saris, F., Hannah, D. M., and Eastwood, W. J., 2010, Spatial variability of precipitation regimes over Turkey: Hydrological Sciences Journal, v. 55, no. 2, p. 234-249.

Schemmel, F., Mikes, T., Rojay, B., and Mulch, A., 2013, The impact of topography on isotopes in precipitation across the central anatolian plateau (Turkey): American Journal of Science, v. 313, no. 2, p. 61-80.

Scholz, D., and Hoffmann, D. L., 2011, StalAge - An algorithm designed for construction of speleothem age models: Quaternary Geochronology, v. 6, no. 3-4, p. 369-382.

Scholz, D., Tolzmann, J., Hoffmann, D. L., Jochum, K. P., Spötl, C., and Riechelmann, D. F. C., 2014, Diagenesis of speleothems and its effect on the accuracy of 230Th/U-ages: Chemical Geology, v. 387, no. 1, p. 74-86.

Sinopoli, G., Masi, A., Regattieri, E., Wagner, B., Francke, A., Peyron, O., and Sadori, L., 2018, Palynology of the Last Interglacial Complex at Lake Ohrid: palaeoenvironmental and palaeoclimatic inferences: Quaternary Science Reviews, v. 180, p. 177-192.

Spanos, S., Maheras, P., Karacostas, T., and Pennas, P., 2003, Objective climatology of 500-hPa cyclones in central and east mediterranean region during warm-dry period of the year: Theoretical and Applied Climatology, v. 75, no. 3-4, p. 167-178.

Spötl, C., Unterwurzacher, M., Mangini, A., and Longstaffe, F. J., 2002, Carbonate speleothems in the dry, inneralpine Vinschgau Valley, Northernmost Italy: Witnesses of changes in climate and hydrology since the Last Glacial Maximum: Journal of Sedimentary Research, v. 72, no. 6, p. 793-808.

Steffensen, J. P., Andersen, K. K., Bigler, M., Clausen, H. B., Dahl-Jensen, D., Fischer, H., Goto-Azuma, K., Hansson, M., Johnsen, S. J., Jouzel, J., Masson-Delmotte, V., Popp, T., Rasmussen, S. O., Röthlisberger, R., Ruth, U., Stauffer, B., Siggaard-Andersen, M. L., Sveinbjörnsdóttir, Á. E., Svensson, A., and White, J. W. C., 2008, High-resolution greenland ice core data show abrupt climate change happens in few years: Science, v. 321, no. 5889, p. 680-684.

Tarutani, T., Clayton, R. N., and Mayeda, T. K., 1969, The effect of polymorphism and magnesium substitution on oxygen isotope fractionation between calcium carbonate and water: Geochimica et Cosmochimica Acta, v. 33, no. 8, p. 987-996.

Toucanne, S., Angue Minto'o, C. M., Fontanier, C., Bassetti, M. A., Jorry, S. J., and Jouet, G., 2015, Tracking rainfall in the northern Mediterranean borderlands during sapropel deposition: Quaternary Science Reviews, v. 129, p. 178-195.

Tremaine, D. M., Froelich, P. N., and Wang, Y., 2011, Speleothem calcite farmed in situ: Modern calibration of $\delta^{18}O$ and $\delta^{13}C$ paleoclimate proxies in a continuously-monitored natural cave system: Geochimica et Cosmochimica Acta, v. 75, no. 17, p. 4929-4950.

Türkeş, M., 1998, Influence of geopotential heights, cyclone frequency and Southern Oscillation on rainfall variations in Turkey: International Journal of Climatology, v. 18, no. 6, p. 649-680.

Türkeş, M., and Erlat, E., 2003, Precipitation changes and variability in Turkey linked to the North Atlantic oscillation during the period 1930-2000: International Journal of Climatology, v. 23, no. 14, p. 1771-1796.

Türkeş, M., Koç, T., and Sariş, F., 2008, Spatiotemporal variability of precipitation total series over Turkey: International Journal of Climatology, v. 29, no. 8, p. 1056-1074.

Tzedakis, C., 2003, Timing and duration of Last Interglacial conditions in Europe: A chronicle of a changing chronology: Quaternary Science Reviews, v. 22, no. 8-9, p. 763-768.

Tzedakis, P. C., Drysdale, R. N., Margari, V., Skinner, L. C., Menviel, L., Rhodes, R. H., Taschetto, A. S., Hodell, D. A., Crowhurst, S. J., Hellstrom, J. C., Fallick, A. E., Grimalt, J. O., McManus, J. F., Martrat, B., Mokeddem, Z., Parrenin, F., Regattieri, E., Roe, K., and Zanchetta, G., 2018, Enhanced climate instability in the North Atlantic and southern Europe during the Last Interglacial: Nature Communications, v. 9, no. 1.

Tzedakis, P. C., McManus, J. F., Hooghiemstra, H., Oppo, D. W., and Wijmstra, T. A., 2003, Comparison of changes in vegetation in northeast Greece with records of climate variability on orbital and suborbital frequencies over the last 450 000 years: Earth and Planetary Science Letters, v. 212, no. 1-2, p. 197-212.

Unal-Imer, E., Shulmeister, J., Zhao, J. X., Tonguc Uysal, I., Feng, Y. X., Duc Nguyen, A., and Yuce, G., 2015, An 80 kyr-long continuous speleothem record from Dim Cave, SW Turkey with paleoclimatic implications for the Eastern Mediterranean: Scientific Reports, v. 5, p. 13560.

Ünal-Imer, E., Shulmeister, J., Zhao, J. X., Uysal, I. T., and Feng, Y. X., 2016, High-resolution trace element and stable/radiogenic isotope profiles of late Pleistocene to Holocene speleothems from Dim Cave, SW Turkey: Palaeogeography, Palaeoclimatology, Palaeoecology, v. 452, p. 68-79.

Verheyden, S., Nader, F. H., Cheng, H. J., Edwards, L. R., and Swennen, R., 2008, Paleoclimate reconstruction in the Levant region from the geochemistry of a Holocene stalagmite from the Jeita cave, Lebanon: Quaternary Research, v. 70, no. 3, p. 368-381.

Von Grafenstein, U., Erlenkeuser, H., Brauer, A., Jouzel, J., and Johnsen, S. J., 1999, A mid-European decadal isotope-climate record from 15,500 to 5000 years B.P: Science, v. 284, no. 5420, p. 1654-1657.

Walker, M., Johnsen, S., Rasmussen, S. O., Popp, T., Steffensen, J. P., Gibbard, P., Hoek, W., Lowe, J., Andrews, J., Björck, S., Cwynar, L. C., Hughen, K., Kershaw, P., Kromer, B., Litt, T., Lowe, D. J., Nakagawa, T., Newnham, R., and Schwander, J., 2009, Formal definition and dating of the GSSP (Global Stratotype Section and Point)

for the base of the Holocene using the Greenland NGRIP ice core, and selected auxiliary records: Journal of Quaternary Science, v. 24, no. 1, p. 3-17.
Wang, Y. J., Cheng, H., Edwards, R. L., An, Z. S., Wu, J. Y., Shen, C. C., and Dorale, J. A., 2001, A high-resolution absolute-dated late pleistocene monsoon record from Hulu Cave, China: Science, v. 294, no. 5550, p. 2345-2348.
Wassenburg, J. A., Immenhauser, A., Richter, D. K., Jochum, K. P., Fietzke, J., Deininger, M., Goos, M., Scholz, D., and Sabaoui, A., 2012, Climate and cave control on Pleistocene/Holocene calcite-to-aragonite transitions in speleothems from Morocco: Elemental and isotopic evidence: Geochimica et Cosmochimica Acta, v. 92, p. 23-47.
Zanchetta, G., Bar-Matthews, M., Drysdale, R. N., Lionello, P., Ayalon, A., Hellstrom, J. C., Isola, I., and Regattieri, E., 2014, Coeval dry events in the central and eastern Mediterranean basin at 5.2 and 5.6ka recorded in Corchia (Italy) and Soreq caves (Israel) speleothems: Global and Planetary Change, v. 122, p. 130-139.
Zanchetta, G., Regattieri, E., Giaccio, B., Wagner, B., Sulpizio, R., Francke, A., Vogel, H., Sadori, L., Masi, A., Sinopoli, G., Lacey, J. H., Leng, M. J., and Leicher, N., 2016, Aligning and synchronization of MIS5 proxy records from Lake Ohrid (FYROM) with independently dated Mediterranean archives: Implications for DEEP core chronology: Biogeosciences, v. 13, no. 9, p. 2757-2768.
Zhou, H., Feng, Y. x., Zhao, J. x., Shen, C. C., You, C. F., and Lin, Y., 2009, Deglacial variations of Sr and $^{87}Sr/^{86}Sr$ ratio recorded by a stalagmite from Central China and their association with past climate and environment: Chemical Geology, v. 268, no. 3-4, p. 233-247.
Ziegler, M., Tuenter, E., and Lourens, L. J., 2010, The precession phase of the boreal summer monsoon as viewed from the eastern Mediterranean (ODP Site 968): Quaternary Science Reviews, v. 29, p. 1481-1490.

Rowe et al.: Multi-proxy speleothem record of climate instability during the early last interglacial in southern Turkey

Figure Captions

Figure 1. (a) Location of sites referred to in the text: 1. Bourgeois-Delaunay Cave; 2. Schneckenloch Cave; 3. Core MD01-2444; 4. Core ODP976; 5. Corchia Cave and Tana che Urla (TCU) Cave; 6. Lago Grande di Monticchio; 7. Tenaghi Phillipon; 8. Dim Cave; 9. Soreq Cave. (b) Location of Dim Cave; note proximity to coast; (c) Plan of Dim Cave (http://www.dimcave.com.tr/magara.htm).

Figure 2. (a) Section through stalagmite Dim 1. Solid line follows the corrosion surface and dashed line the onset of mixed mineralogy (see below). Dotted lines follow stable isotope sampling tracks. Note occasional shifts of growth axis. Filled ovals show locations of U/Th dated samples. Open red ovals are locations of dated samples from a different face projected onto this section. Black rectangle encloses the scanned area of an adjacent slab shown in fig. 2b. (b) Scanned slab of the upper 230 mm of Dim 1, offset from the central growth axis. The darker grey colours are calcite, while the paler, cream colours are either aragonite or mixed aragonite/calcite. Note the clear stalagmite top morphologies at 131 mm dft. A prominent band of paler, creamy carbonate (mixed aragonite and calcite) is present (white arrow) between 103 and 87 mm dft. The upper surface of this band displays a clear corrosion surface (CS) and above this surface (RHS of image) there is a 10 mm zone where aragonite near the flanks (black arrow) appears to be replaced by darker calcite in the axial zone. The growth axis is offset (GAO) by ~20 mm above the corrosion surface. Flanking layers are mainly aragonite mineralogy (AFL).

Figure 3. Dim 1 thin section photomicrographs; all are crossed polarised images with scale bars of 500 µm length. a) Columnar compact (C) calcite, typical of the lower part of the stalagmite. The primary calcite fabrics are inclusion poor with length to width ratios approaching elongated columnar (Ce) fabric. b) Sharp lower boundary (axial part ~103 mm) to zone of mixed aragonite and calcite showing bundles of acicular aragonite that nucleated directly on underlying columnar crystal terminations. c) As b) showing spaces between aragonite bundles filled with non-orientated aragonite needles. White arrow points to 1 mm high 'step' in the boundary, formed by dissolution, where C calcite shows a sharp change to aragonite needle fabrics (right of arrow tip). d) Detail of mineralogical change shown in c) where the near vertical dissolution surface cuts primary C calcites, and primary aragonite needle fabrics have grown adjacent to the sub-vertical surface.

Figure 4. Dim 1 thin section micrographs. a) Crossed polarised image of vertical transitions from calcite (c) to aragonite needle fabrics (a) in the zone of mixed aragonite and calcite. There is little evidence for neomorphism and the fabrics are interpreted as indicative of syn-depositional switching of primary mineralogies; scale bar is 500µm. b) Crossed polarised image of mostly aragonite needle fabrics in the upper part of the zone of mixed aragonite and calcite. Note two inclusion trails marked by arrows which can be traced laterally from calcite (upper left) into aragonite. The boundary between the top most aragonite layer and the overlying C calcites can be seen at top right of the image; scale bar is 500 µm. c) Crossed polarised image showing detail of the upper boundary between aragonite and overlying C calcites. Note the ragged terminations to aragonite needles, and presence of a zone of equant microspar (EM) directly above the boundary, and in places between aragonite needles. Faint inclusion trails are again evident in the aragonite; scale bar is 500 µm. d) Plane light image of flank zone aragonite spherulite fabrics (whole field of view) forming a clumped texture. Scale bar is 1 mm.

Figure 5. Dim 1 thin section photomicrographs. a) Crossed polarised image showing detail of irregular upper boundary (white arrows) between spherulitic aggregates of aragonite (a) needle crystals and overlying neomorphic mosaic calcites (c) in the flank zone; scale bar is 500 µm. Plane light images of: b) linear inclusion trails in Co calcites making prominent dark lines and layers; c) spherical fluid inclusions in a linear trail; d) inclusion trails associated with relict aragonite needle fabrics (arrow); and e) dark sub-horizontal layers defining terminations of underlying Co calcite crystals. Scale bars are 500 µm.

Figure 6. (a) $\delta^{18}O$, (b) $\delta^{13}C$ and (c) $^{87}Sr/^{86}Sr$ data vs. distance from top of Dim 1. Heavy lines in (a) and (b) are 5-point running means. Vertical dashed line marks the position of the corrosion surface. Vertical grey shading shows region of mixed aragonite-calcite mineralogy. Heavy vertical black bars in (a) and (b) show range of modern values measured in active aragonite straw stalactites.

Figure 7. $^{87}Sr/^{86}Sr$ values of likely sources contributing to the Dim 1 signal. Saharan dust, with a value of ~0.7200, is not plotted. The upper end member represents the combined composition of all input components except limestone bedrock (Supplementary Material).

Figure 8. Age - depth relationship derived from StalAge (Scholz and Hoffmann, 2011) using 14 dated samples shown by petrographic analyses not to have experienced post-depositional modification (see Table 1 and text for discussion). Horizontal dashed line shows location of hiatus. ♦ denotes aragonite samples.

Figure 9. Relationship between $(^{234}U/^{238}U)_0$ and $\delta^{18}O$ along the Dim 1 growth axis. Uranium isotope ratio errors are within symbol perimeters. Trend line is a fifth order polynomial to highlight the general data pattern. Vertical axes are inverted.

Figure 10. (a) $\delta^{18}O$, (b) $\delta^{13}C$ and (c) $^{87}Sr/^{86}Sr$ data plotted on the Dim 1 U-series timescale. Heavy line is 5-point running mean.

Figure 11. Relationship of Dim 1 $\delta^{18}O$ and $\delta^{13}C$ records to other contemporaneous paleoclimatic archives encompassing the penultimate glacial-interglacial transition. Records are plotted on their own timescales. (a) Dim 1 $\delta^{18}O$ record; black bar represents typical 2σ errors on U-Th dates (±~0.7 ka); (b) Dim 1 $\delta^{13}C$ record; (c) $\delta^{18}O$ profile from speleothem CC5, Corchia Cave, N.W. Italy (Drysdale et al., 2009); (d) $\delta^{18}O$ record from stalagmite D4, Dongge Cave, China (Kelly et al., 2006); (e) $\delta^{18}O$ record from Bourgeois-Delaunay Cave, southwest France (Couchoud et al., 2009); (f) Mg/Ca SST record from marine core ODP976, Alboran Sea (Jiminez-Amat and Zahn, 2014); (g) Alkenone SST record from marine core ODP976 (Marino et al., 2015); (h) $\delta^{18}O$ G. Bulloides record from marine core ODP976 (Jiminez-Amat and Zahn, 2014). Blue vertical line: termination of Heinrich Event 11 at 130 ka (Marino et al., 2015); Pink line: onset of East Asia Monsoon at 129.0 ka (Kelly et al., 2006; Cheng et al., 2009); Green line: base of sapropel S5 at 128.3 ka (Grant et al., 2016). Black dashed lines link the Dim 1 positive $\delta^{18}O$ event to suggested correlatives in European and Chinese speleothem records.

Figure 12. Positive $\delta^{18}O$ anomalies in speleothems from Schneckenloch Cave (Moseley et al., 2015), Dim Cave (this study) and BD Cave (Couchoud et al., 2009). Schneckenloch and BD data are plotted on their own timescales; Dim data has been tuned to the BD timescale using $\delta^{18}O$ peaks in the isotopic profiles as tie points (Fig. S8). The events are synchronous within U-series dating errors.

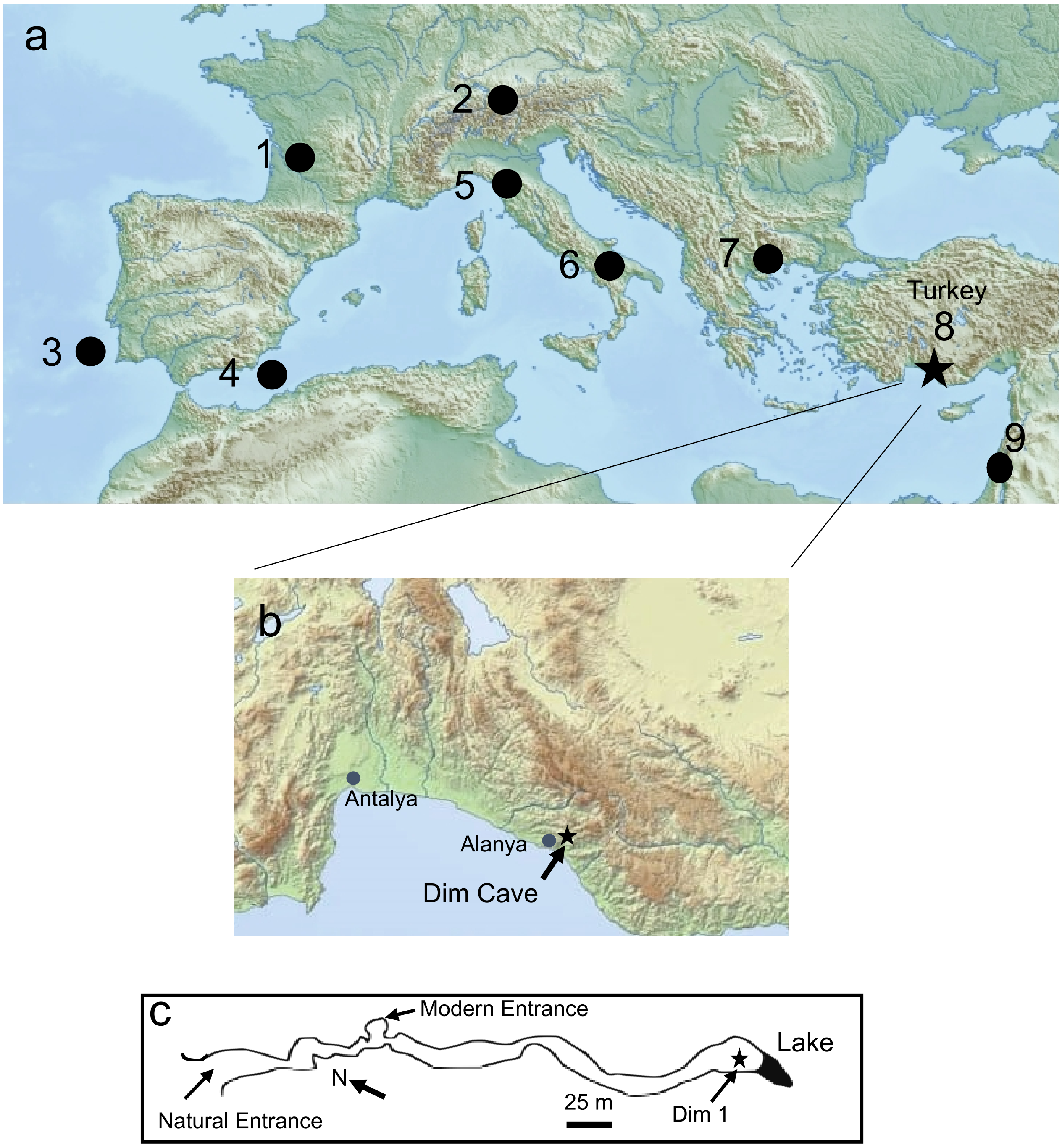
a
1
2
3
4
5
6
7
Turkey
8
9
b
Antalya
Alanya
Dim Cave
c
Modern Entrance
Lake
Natural Entrance
N
25 m
Dim 1

Figure 1

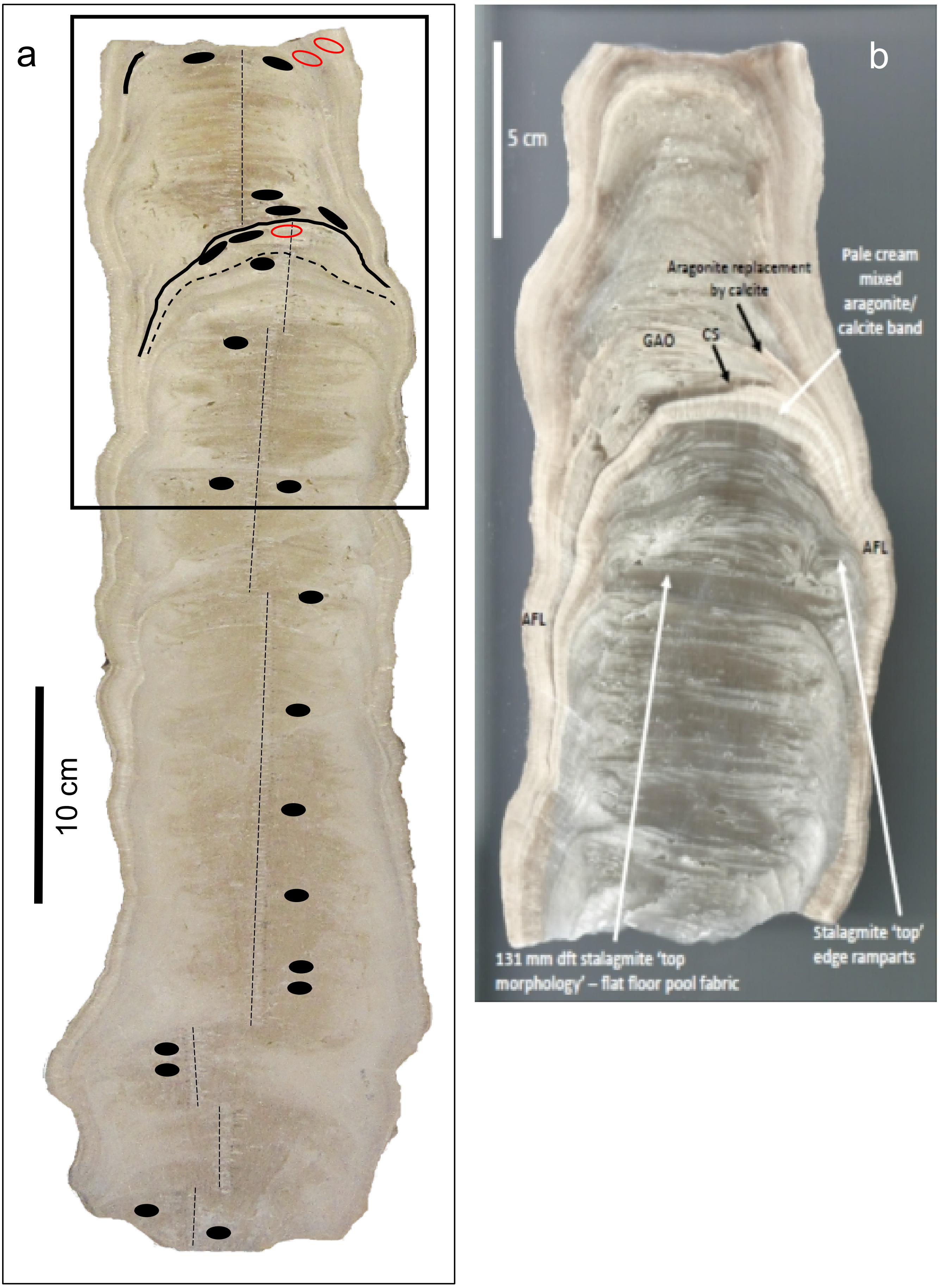
a
10 cm
b
5 cm
Aragonite replacement by calcite
Pale cream mixed aragonite/ calcite band
GAO
CS
AFL
AFL
131 mm dft stalagmite 'top morphology' – flat floor pool fabric
Stalagmite 'top' edge ramparts

Figure 2

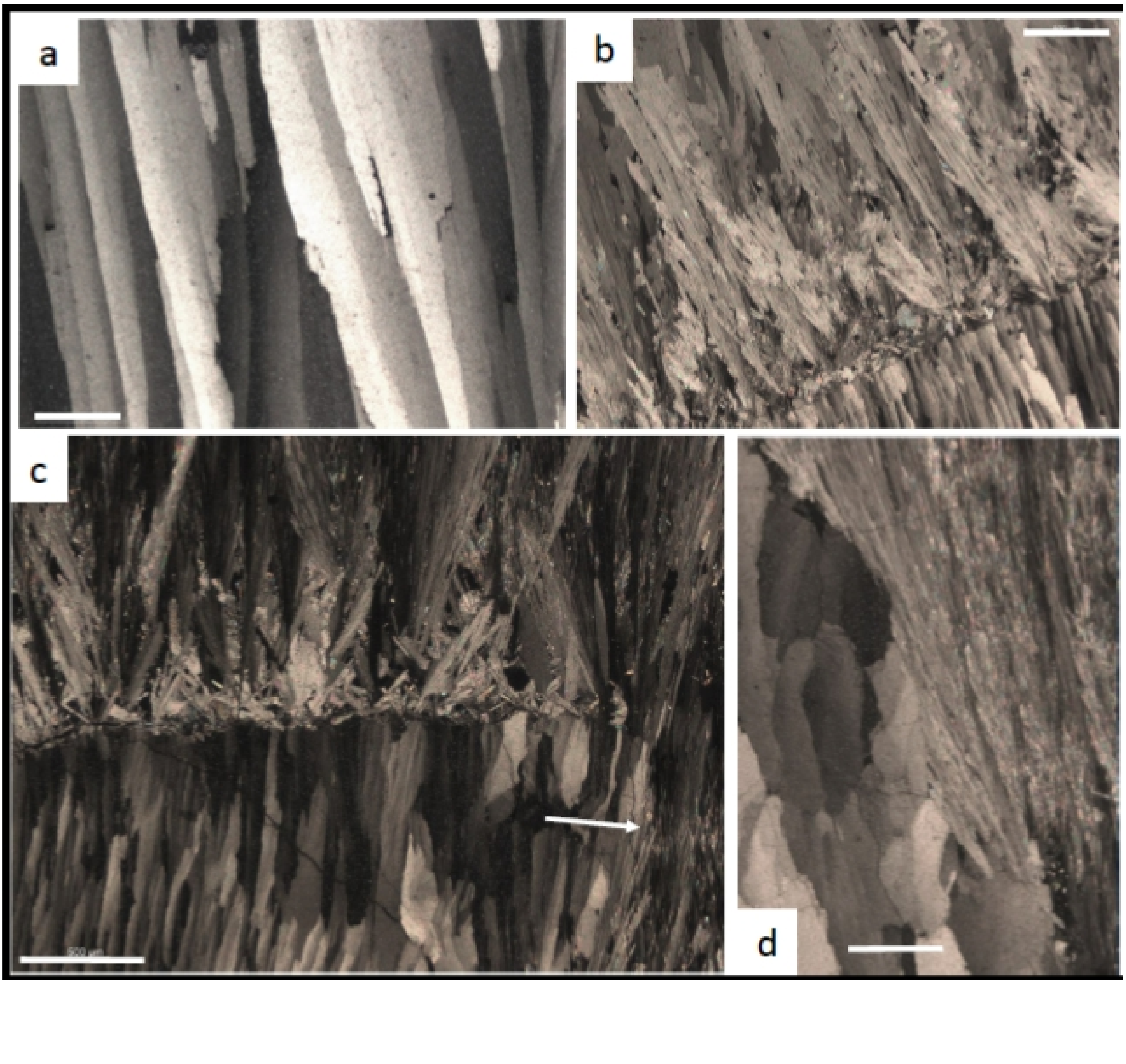

Figure 3

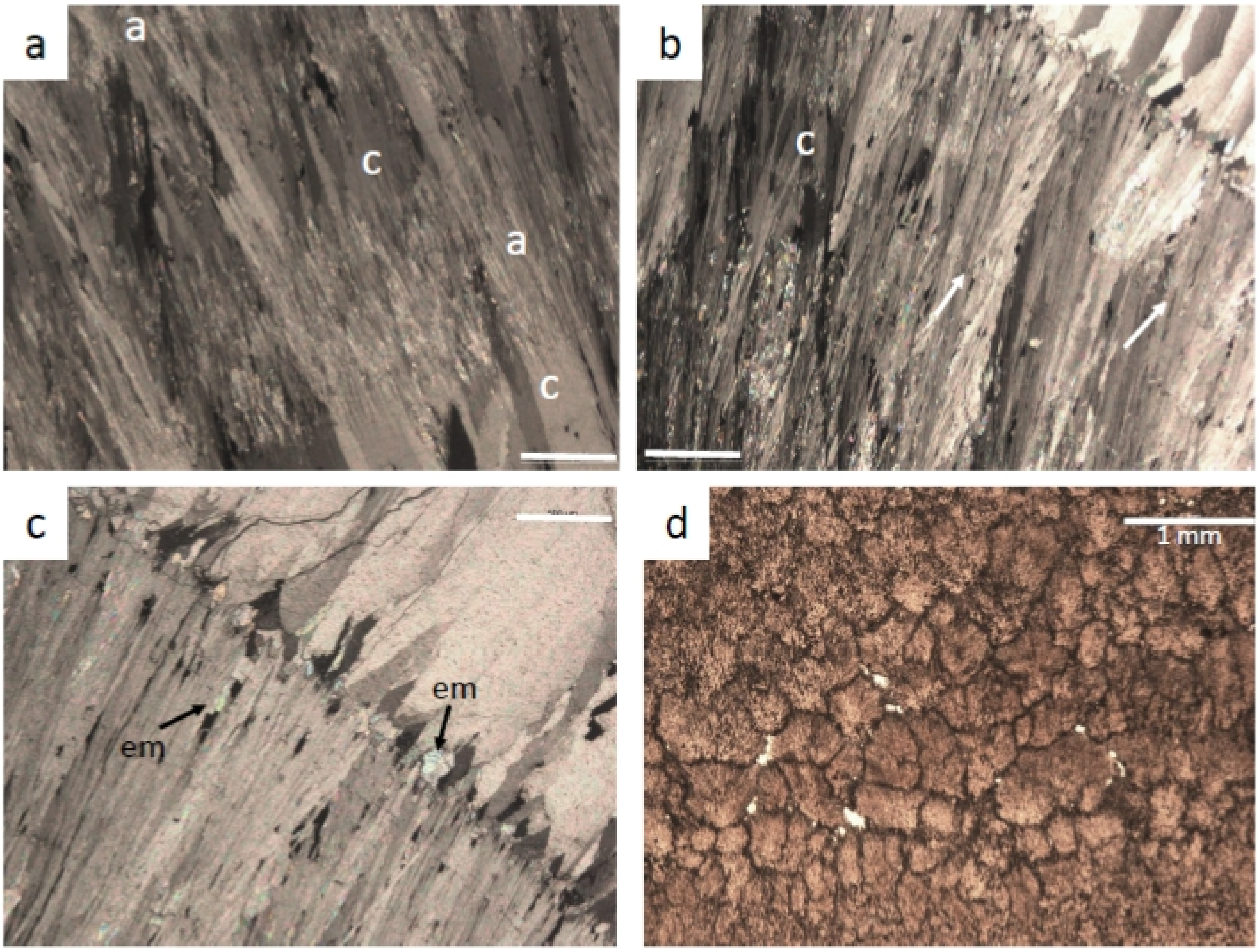

Figure 4

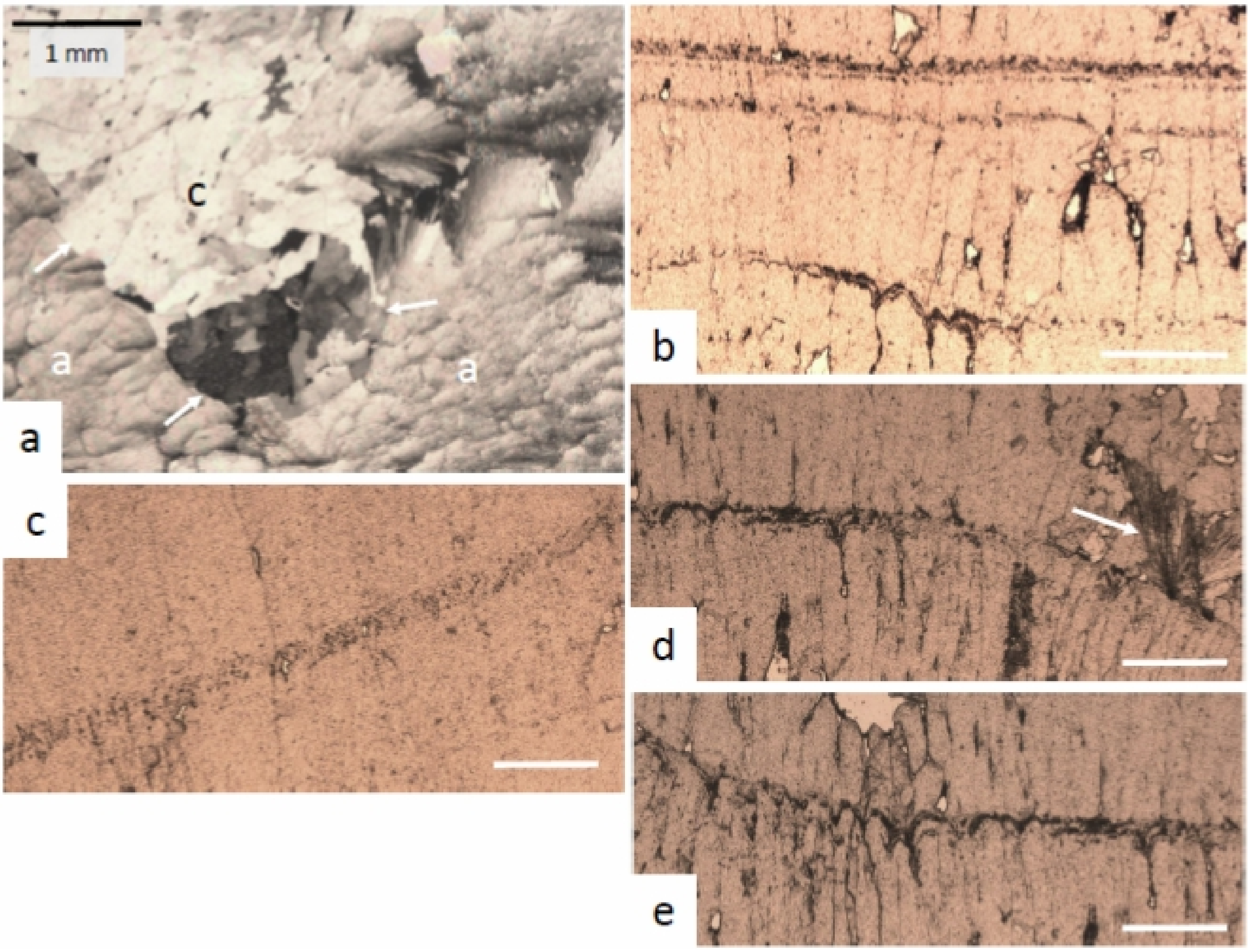

Figure 5

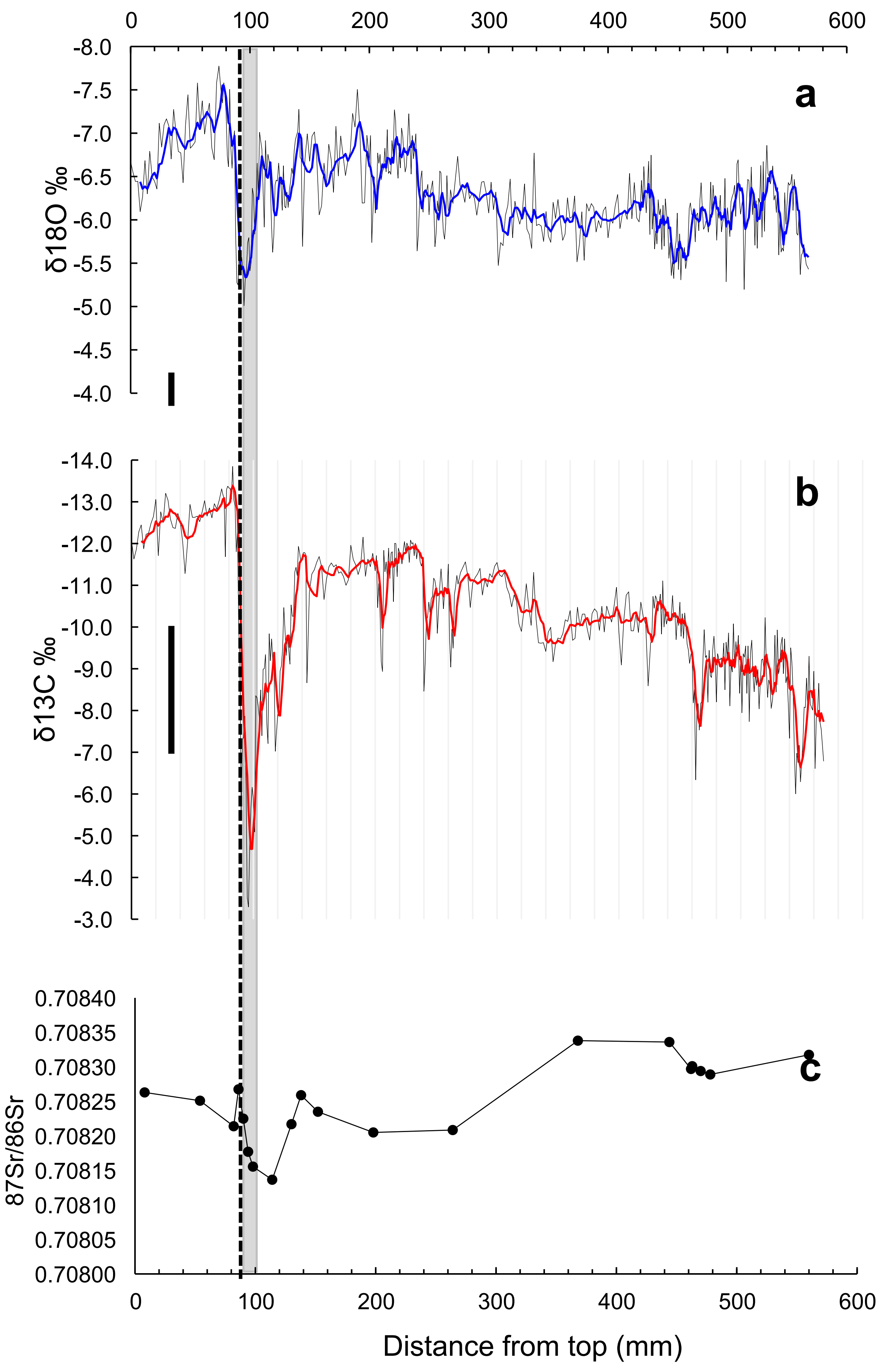

0
100
200
300
400
500
600
-8.0
-7.5
-7.0
-6.5
-6.0
-5.5
-5.0
-4.5
-4.0
δ18O ‰
a
-14.0
-13.0
-12.0
-11.0
-10.0
-9.0
-8.0
-7.0
-6.0
-5.0
-4.0
-3.0
δ13C ‰
b
0.70840
0.70835
0.70830
0.70825
0.70820
0.70815
0.70810
0.70805
0.70800
87Sr/86Sr
c
0
100
200
300
400
500
600
Distance from top (mm)

Figure 6

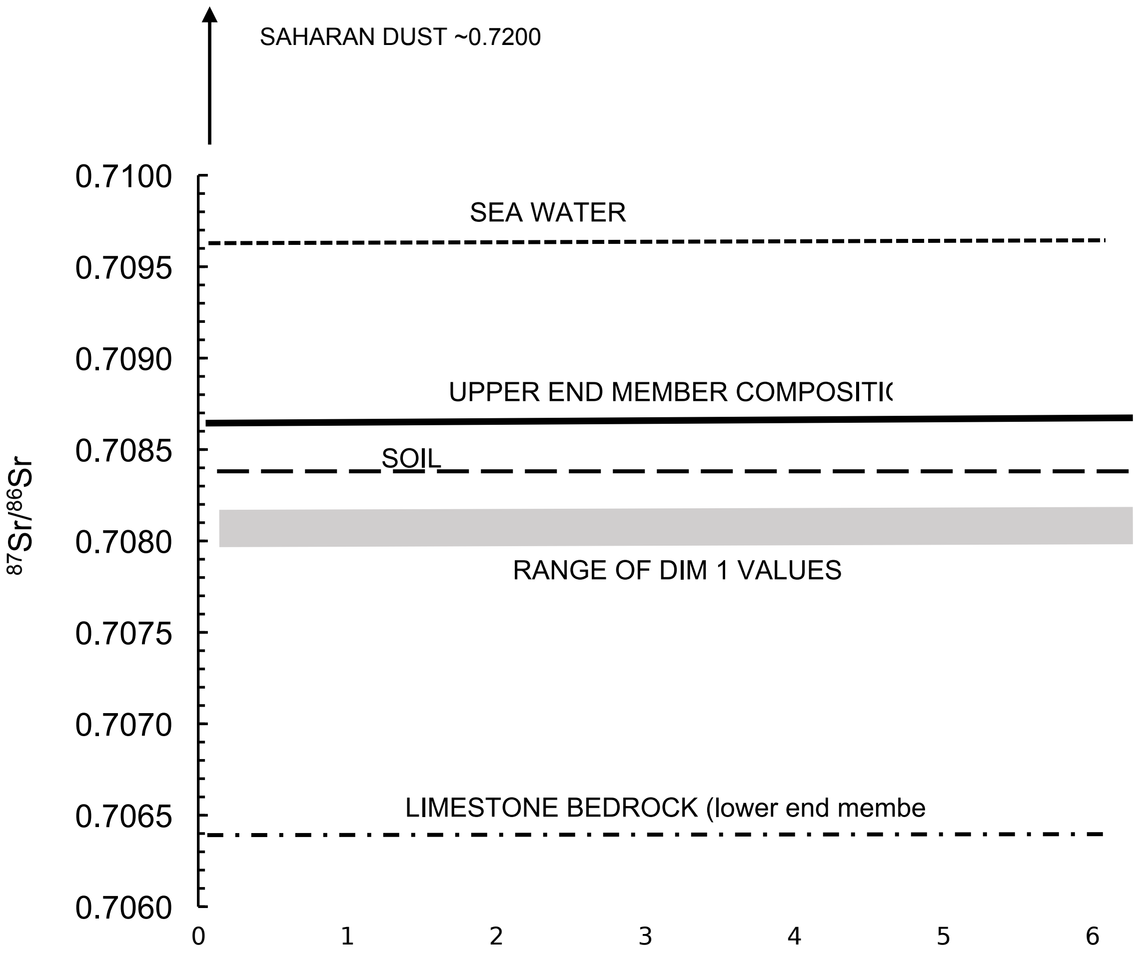
SAHARAN DUST ~0.7200
0.7100
SEA WATER
0.7095
0.7090
UPPER END MEMBER COMPOSITI(
0.7085
SOIL
0.7080
RANGE OF DIM 1 VALUES
0.7075
0.7070
LIMESTONE BEDROCK (lower end membe
0.7065
0.7060
0
1
2
3
4
5
6
$^{87}Sr/^{86}Sr$

Figure 7

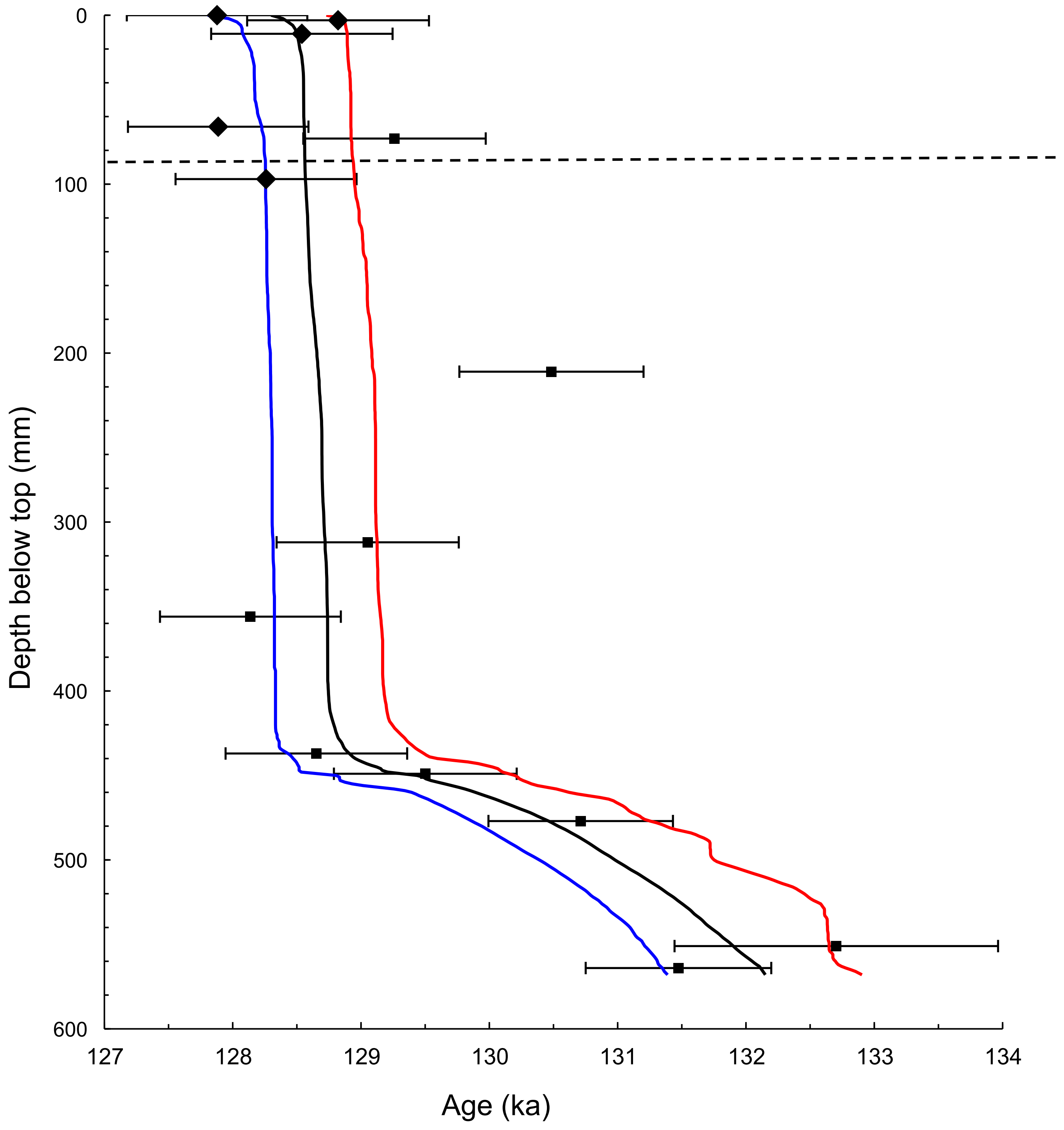

Depth below top (mm)
0
100
200
300
400
500
600
127
128
129
130
131
132
133
134
Age (ka)

Figure 8

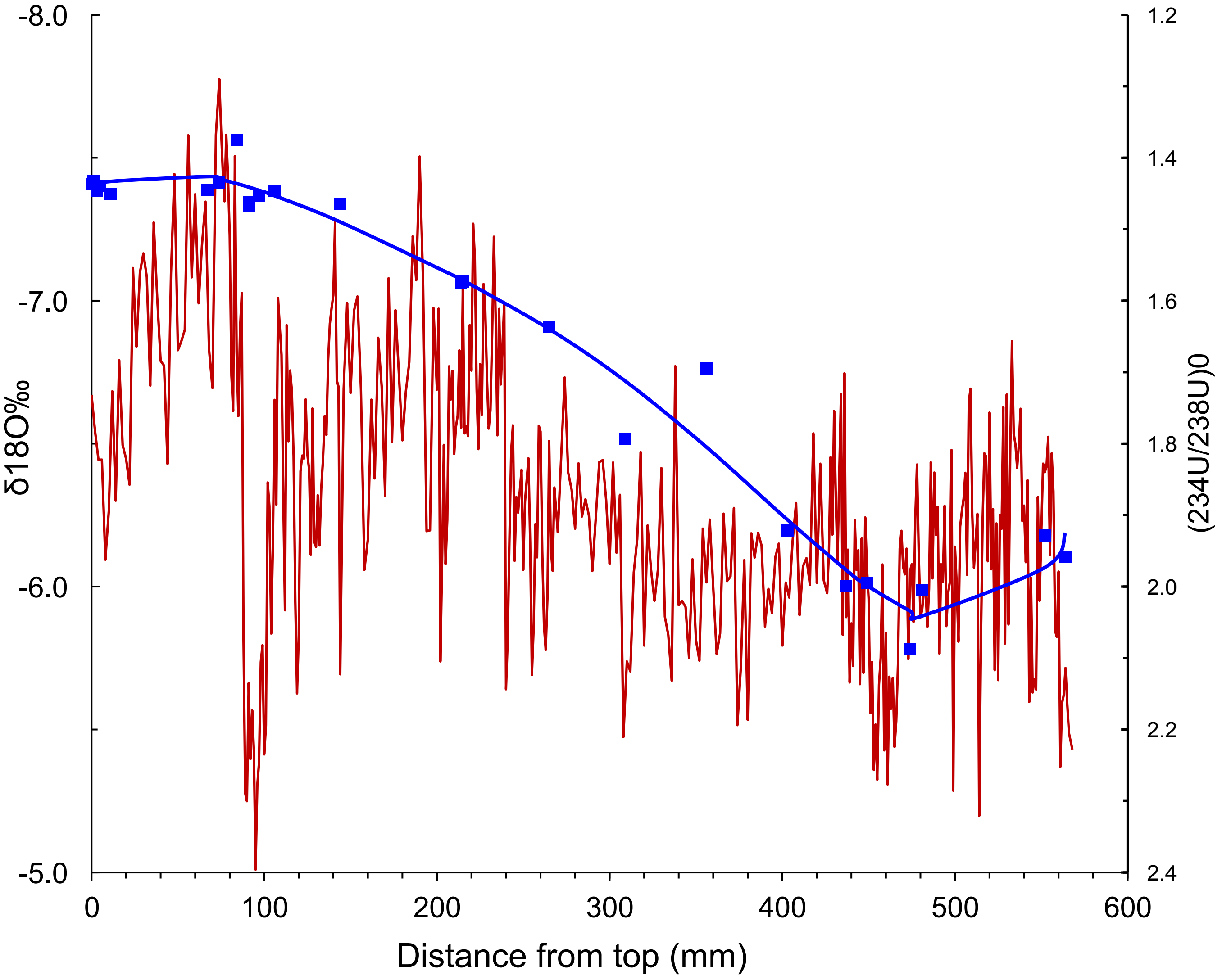

-8.0
-7.0
-6.0
-5.0
δ18O‰
1.2
1.4
1.6
1.8
2.0
2.2
2.4
(234U/238U)0
0
100
200
300
400
500
600
Distance from top (mm)

Figure 9

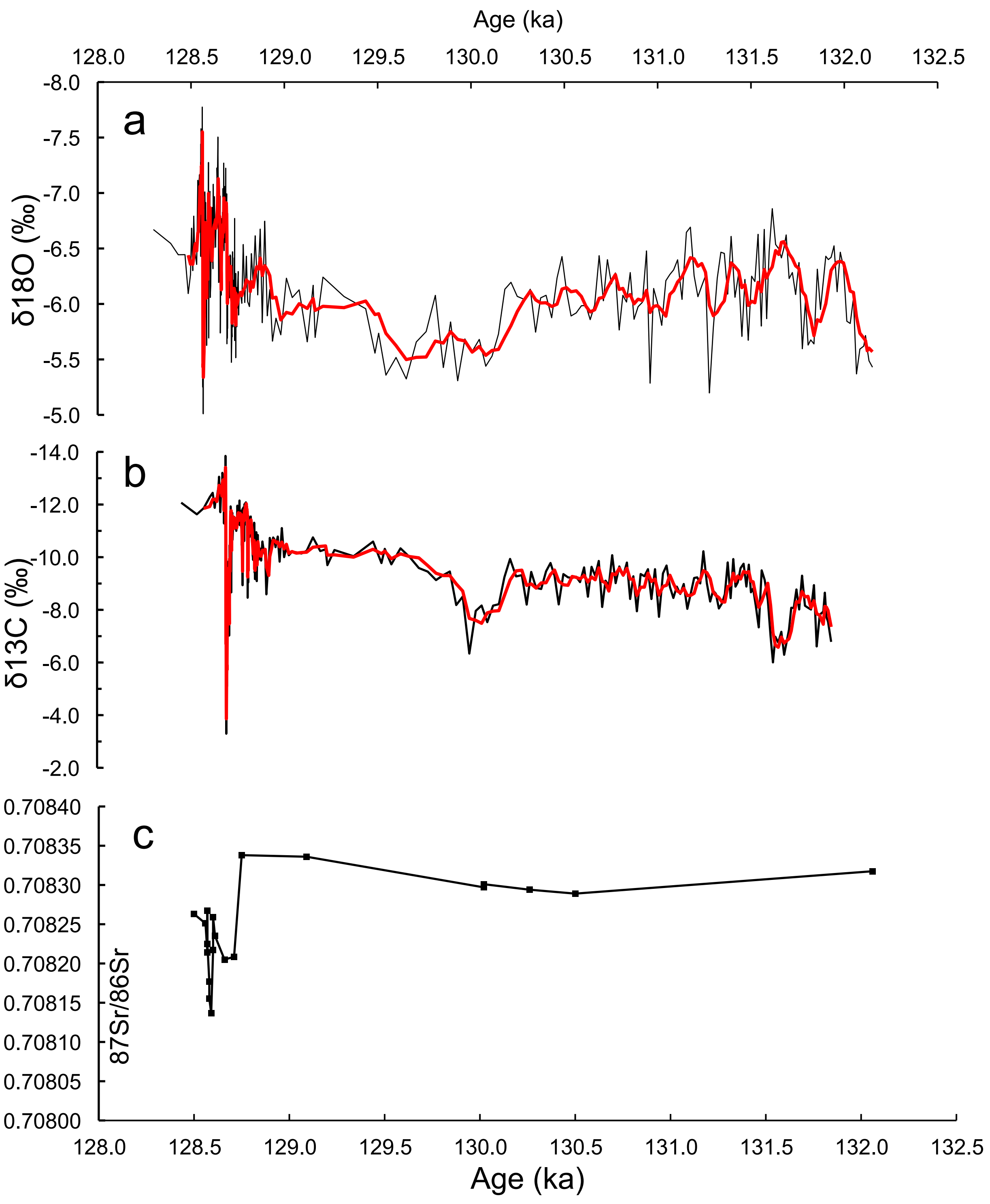

Age (ka)
128.0
128.5
129.0
129.5
130.0
130.5
131.0
131.5
132.0
132.5
a
δ18O (‰)
-8.0
-7.5
-7.0
-6.5
-6.0
-5.5
-5.0
b
δ13C (‰)
-14.0
-12.0
-10.0
-8.0
-6.0
-4.0
-2.0
c
87Sr/86Sr
0.70840
0.70835
0.70830
0.70825
0.70820
0.70815
0.70810
0.70805
0.70800
Age (ka)

Figure 10

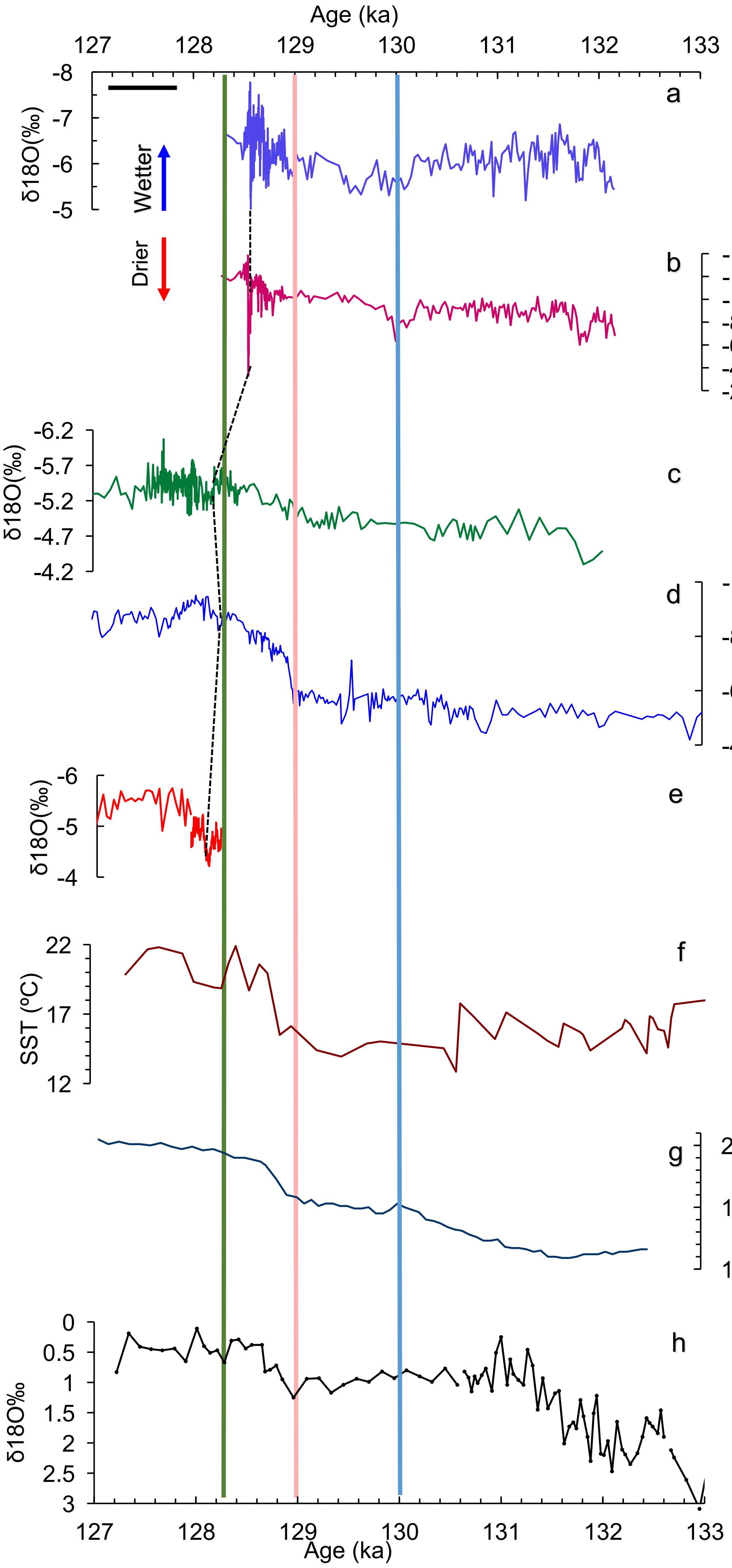
Age (ka)
127
128
129
130
131
132
133
-8
-7
-6
-5
δ18O(‰)
a
Wetter
Drier
b
-14
-12
-10
-8
-6
-4
-2
δ13C(‰)
-6.2
-5.7
-5.2
-4.7
-4.2
δ18O(‰)
c
d
-10
-8
-6
-4
δ18O(‰)
-6
-5
-4
δ18O(‰)
e
22
17
12
SST (ºC)
f
g
21
16
11
SST (ºC)
0
0.5
1
1.5
2
2.5
3
δ18O‰
h
127
128
129
130
131
132
133
Age (ka)

Figure 11

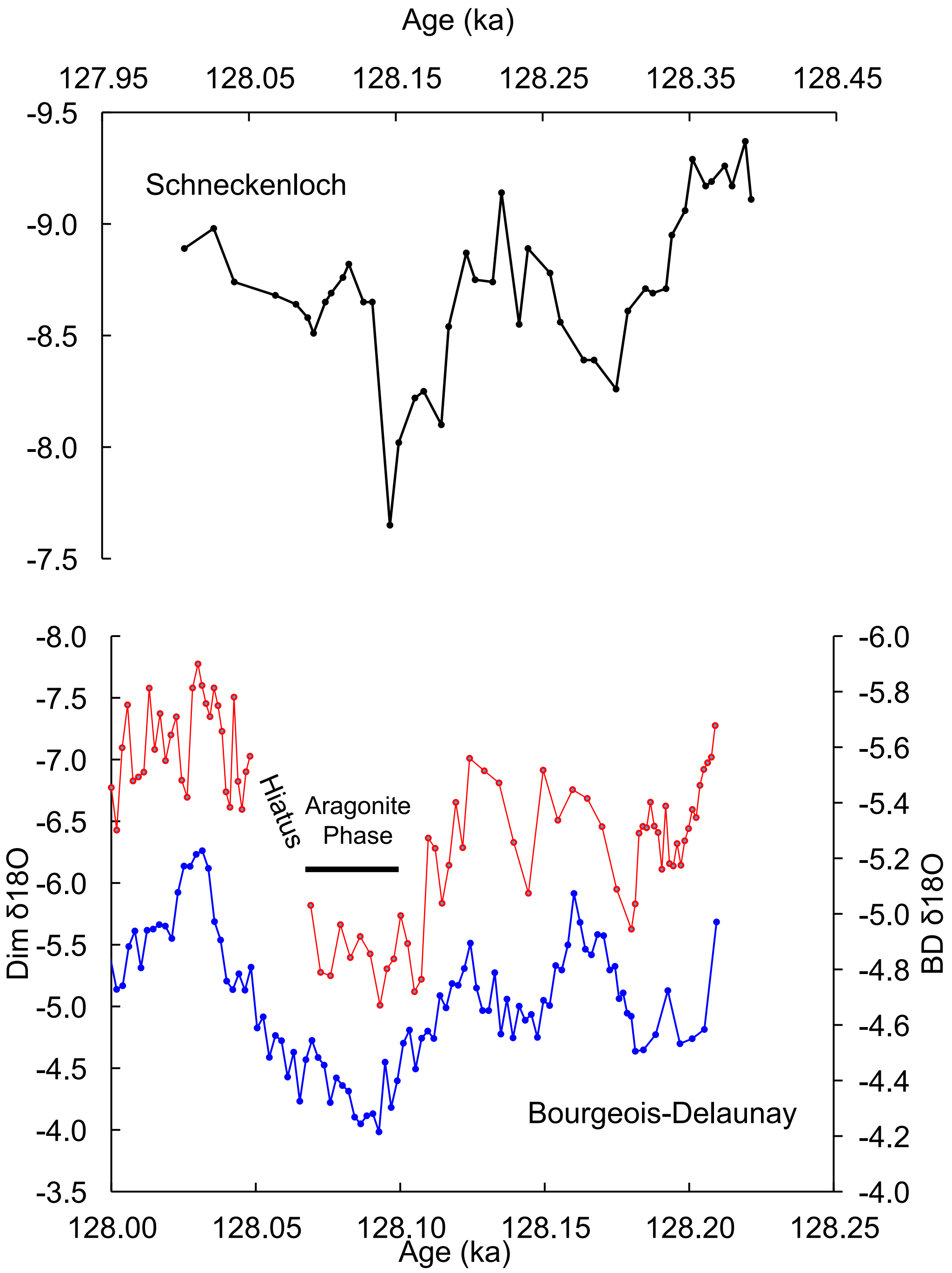

Age (ka)
127.95
128.05
128.15
128.25
128.35
128.45
-9.5
-9.0
-8.5
-8.0
-7.5
Schneckenloch
-8.0
-7.5
-7.0
-6.5
-6.0
-5.5
-5.0
-4.5
-4.0
-3.5
Dim δ18O
Hiatus
Aragonite
Phase
-6.0
-5.8
-5.6
-5.4
-5.2
-5.0
-4.8
-4.6
-4.4
-4.2
-4.0
BD δ18O
Bourgeois-Delaunay
128.00
128.05
128.10
128.15
128.20
128.25
Age (ka)

Figure 12

Rowe et al. Table Caption

Table 1. U-series dating results for stalagmites Dim 1 and Dim 3. Samples excluded from Dim 1 age modelling are shaded. Aragonite samples are in bold. Underlined laboratory ID numbers identify samples in which indications of corrosion have been observed in thin section petrography. Corrected ages BP are before 1950; corrections for detrital contamination are <0.1 ka. AR = Activity ratio.

Table 1.

Lab ID	Distance from top [mm]	U [ppm]	^{232}Th [ppb]	^{230}Th/ ^{238}U AR	^{234}U/ ^{238}U AR	(^{234}U/^{238}U)$_0$ AR	^{230}Th/^{232}Th AR	Age uncorrected [ka]	±2σ	Age corrected [ka BP]	±2σ
						Dim 1					
52-3	**0**	**1.06**	**0.925**	**0.9348(26)**	**1.3043(14)**	**1.4365(19)**	**3266.0**	**127.896**	**0.688**	**127.816**	**0.688**
29-10	1	0.43	0.307	0.89519(24)	1.3100(15)	1.4319(19)	3811.0	117.531	0.588	117.454	0.588
52-2	**3**	**3.28**	**0.681**	**0.9434(25)**	**1.3101(14)**	**1.4461(19)**	**13836.8**	**128.825**	**0.687**	**128.759**	**0.687**
41-8	5	0.42	0.419	0.8985(24)	1.3161(15)	1.4400(19)	2748.2	117.284	0.597	117.201	0.597
52-4	**11**	**4.66**	**0.279**	**0.9448(26)**	**1.3133(15)**	**1.4503(19)**	**48083.1**	**128.540**	**0.689**	**128.477**	**0.689**
52-1	**67**	**6.36**	**3.963**	**0.9400(28)**	**1.3106(15)**	**1.4456(20)**	**4586.8**	**127.899**	**0.741**	**127.825**	**0.741**
37-5	74	0.38	0.749	0.9384(25)	1.3017(14)	1.4345(19)	1462.5	129.302	0.682	129.199	0.681
29-9	84	0.77	0.345	0.9264(27)	1.2552(14)	1.3747(19)	6309.1	136.164	0.809	136.092	0.809
41-6	**91**	**2.50**	**0.179**	**0.9225(24)**	**1.3328(17)**	**1.4666(21)**	**39093.3**	**119.761**	**0.610**	**119.698**	**0.610**
29-7	**91**	**1.86**	**0.374**	**0.91834(23)**	**1.3286(15)**	**1.4605(20)**	**17299.4**	**119.544**	**0.579**	**119.479**	**0.579**
52-5	**97**	**4.14**	**0.988**	**0.9455(25)**	**1.3156(15)**	**1.4532(20)**	**12051.1**	**128.265**	**0.688**	**128.198**	**0.688**
41-5	106	0.25	0.116	0.9227(25)	1.3160(18)	1.4467(22)	6012.2	122.776	0.659	122.704	0.659
41-4	144	0.17	0.190	0.9453(26)	1.3248(20)	1.4641(25)	2589.3	126.462	0.729	126.377	0.728
37-3	214	0.17	0.989	1.0216(34)	1.3980(15)	1.5751(21)	520.3	130.597	0.831	130.422	0.830
33-6	215	0.17	0.265	1.0029(30)	1.4024(18)	1.5734(23)	1955.9	125.531	0.729	125.439	0.729
41-2	265	0.15	0.136	1.0193(28)	1.4527(20)	1.6364(24)	3354.3	120.685	0.642	120.606	0.642
102-2	309	0.15	0.565	1.1388(30)	1.5509(19)	1.7928(25)	923.2	129.114	0.663	128.986	0.665
102-1	356	0.15	0.639	1.0805(29)	1.4841(19)	1.6950(24)	780.4	128.212	0.670	128.072	0.672
41-1	403	0.17	0.170	1.1998(32)	1.6451(23)	1.9213(29)	3565.6	126.312	0.672	126.234	0.672
33-4	437	0.16	0.450	1.2531(35)	1.6952(21)	1.9994(28)	1340.2	128.695	0.696	128.590	0.696
37-1	449	0.19	0.204	1.2540(42)	1.6904(18)	1.9949(28)	3461.8	129.518	0.791	129.439	0.791
37-4	474	0.13	0.176	1.3112(36)	1.7523(19)	2.0879(27)	2852.3	130.732	0.682	130.650	0.682
33-5	481	0.14	0.439	1.2191(38)	1.7162(23)	2.0050(30)	1216.6	120.081	0.681	119.973	0.681
29-6	552	0.10	0.380	1.2289(69)	1.6383(24)	1.9282(42)	1023.0	132.761	1.363	132.642	1.362
37-2	564	0.10	0.266	1.2413(42)	1.6615(18)	1.9586(28)	1430.6	131.515	0.829	131.412	0.828
						Dim 3					
33-9	7	5.29	0.280	0.0799(02)	1.2780(05)	1.2836(05)	4634.3	7.004	0.017	6.939	0.017
33-10	40	5.66	0.230	0.0926(02)	1.2952(14)	1.3020(14)	6858.8	8.045	0.022	7.980	0.022

SUPPORTING ONLINE MATERIAL FOR

Climate instability during the early last interglacial recorded by multiple proxies in a speleothem from southern Turkey

Rowe, P.J.[1*], Wickens, L. B.[1], Sahy, D.[2], Marca, A. D.[1], Peckover, E.[1], Noble, S.[2], Özkul, M.[3], Baykara, M. O.[3], Millar I.L[2], and Andrews, J.E.[1]

*To whom correspondence should be addressed: p.rowe@uea.ac.uk

This File includes:

U-series methods

Strontium Isotope End Member Compositions

Figs S1-S9

References

Speleothem isotope data

Cave water isotope data

1. U-Series Dating Methods:

Dating was carried out at the NERC Isotope Geosciences Laboratory, Keyworth, UK. U isotope data were initially obtained on an Axiom multi-collector inductively coupled mass spectrometer (MC-ICP-MS), but the bulk of the U and Th data were obtained on a Thermo Neptune Plus MC-ICP-MS using an Aridus II desolvating nebulizer and standard-sample bracketing. 200-250 mg samples were dissolved in HNO_3, and spiked with a mixed ^{229}Th-^{236}U tracer and equilibrated overnight. Following oxidation of organics in 15 M HNO_3 and 30% H_2O_2, U and Th were pre-concentrated by Fe co-precipitation using a FeCl solution. Samples were loaded on cleaned and equilibrated columns in 7 M HNO_3 and Th eluted in 8 M HCl followed by U elution in 0.2 M HCl. After an initial separation on AG-1 x 8, the separated Th aliquots were further purified using a second pass through AG-1 x 8 columns, while separated U was purified on UTEVA columns following Andersen et al. (2008). The U and Th separates were subjected to repeated oxidation steps and taken up in 1 ml 0.2 M HCl - 0.05 M HF and centrifuged prior to mass spectrometry.

U mass bias correction used measurements of CRM 112a spiked with a $^{233}U/^{236}U$ tracer (IRMM 3636), while SEM gain was monitored using measured $^{234}U/^{235}U$ of mass bias-corrected unspiked CRM 112a analyses. Mass-bias and spike-corrected $^{234}U/^{238}U$ values of the spiked CRM 112a runs were used as a check on the SEM gain. Hydride and tailing corrections followed (Hiess et al., 2012) and were on the order of 2 ppm of the adjacent peaks and very consistent on a timescale of several days. Mass bias and SEM gain for Th measurements were corrected using an in-house ^{229}Th-^{230}Th-^{232}Th reference solution calibrated against CRM 112a. Th isotopes were measured in static multi-collection mode with ^{229}Th and ^{232}Th measured on Faraday detectors and ^{230}Th on an SEM. Total ^{238}U and ^{232}Th blanks were <10 pg and <4 pg and were negligible relative to the sample U and Th. Standard accuracy (within 0.1%) and reproducibility (within 0.2%) of $^{234}U/^{238}U$ was monitored by replicate analyses of Harwell uraninite HU-1. Replicate measurements of the reference solution showed $^{229}Th/^{230}Th$ accuracy and reproducibility to be ± 0.2-0.3% for ^{230}Th ion beams > 5000 cps. Data reduction was carried out using in-house Excel spreadsheets incorporating the revised average $^{235}U/^{238}U$ ratio of 137.818 (Hiess et al., 2012), and U-Th ages were calculated using the decay constants of (Cheng et al., 2013).

2. Strontium Isotope End Member Compositions

If the limestone host rock is considered to be one endmember of a mixing line, a regression line fitted to a plot of $^{87}Sr/^{86}Sr$ vs. 1/Sr concentration and projected to the 1/Sr zero intercept reveals the composition of the other end member (or the integrated composition of multiple other sources) (Ayalon et al., 1999; Goede et al., 1998; Verheyden et al., 2000). Regression of the Dim 1 calcite Sr data and of Dim 1 and Dim 3 aragonite data converge on a ratio of 0.70864. This is more radiogenic than the soil and indicates a contribution from sea spray ($^{87}Sr/^{86}Sr$ = 0.70930) and/or far travelled, probably Saharan, dust ($^{87}Sr/^{86}Sr$ =0.72200, (Cole et al., 2009)). Ratios lie closer to the radiogenic end member than to the limestone and the fractional contribution of that source can be calculated from

$$E = 1- (R_E – R_M) / (R_E – R_L) \quad (5)$$

Where E is the relative input from the exogenic end member, R_E is the Sr-ratio of that end member (0.70864), R_L is the Sr-ratio of the host rock (0.70716) and R_M is the measured Sr ratio of the speleothem sample. E varies from ~0.79 where Sr-ratios are highest between ~440 mm depth and the base to ~0.65 at the minimum value at 114 mm.

3. Supplementary Figures

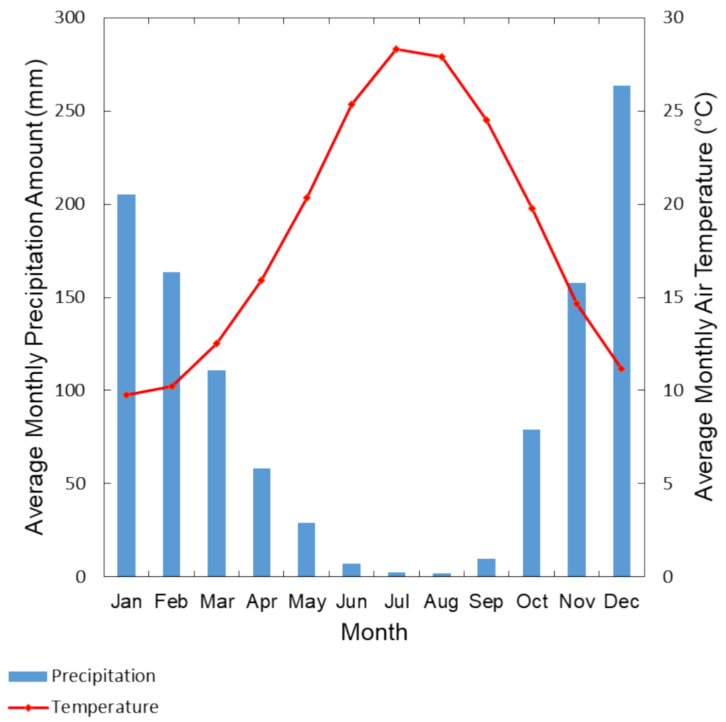

Figure S1. Average monthly rainfall and temperature data for Antalya for period 1963 to 2004. (IAEA/WMO). Rainfall is strongly seasonal with a winter maximum.

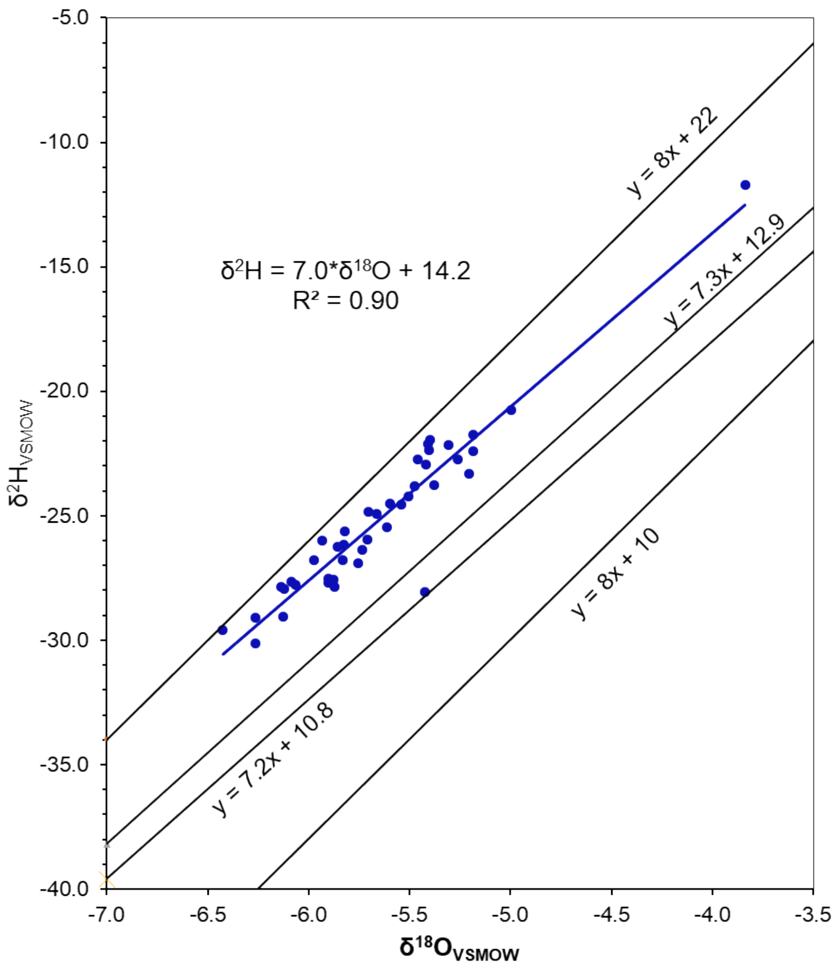

Figure S2. Oxygen and hydrogen isotope relationships for meteoric waters. Dim Cave Data: $\delta^2H = 7.0*\delta^{18}O + 14.2$; Antalya Meteoric Water Line: $\delta D = 7.3*\delta^{18}O + 12.9$ (Dirican et al., 2005); Mediterranean Meteoric Water Line: $\delta D = 8.0*\delta^{18}O + 22$, (Gat and Carmi, 1970); Global Meteoric Water Line: $\delta D = 8.0*\delta^{18}O + 10$, (Craig, 1961); Groundwaters from the southern side of the Taurus Mountains: $\delta D = 7.2*\delta^{18}O + 10.8$, (Schemmel et al., 2005).

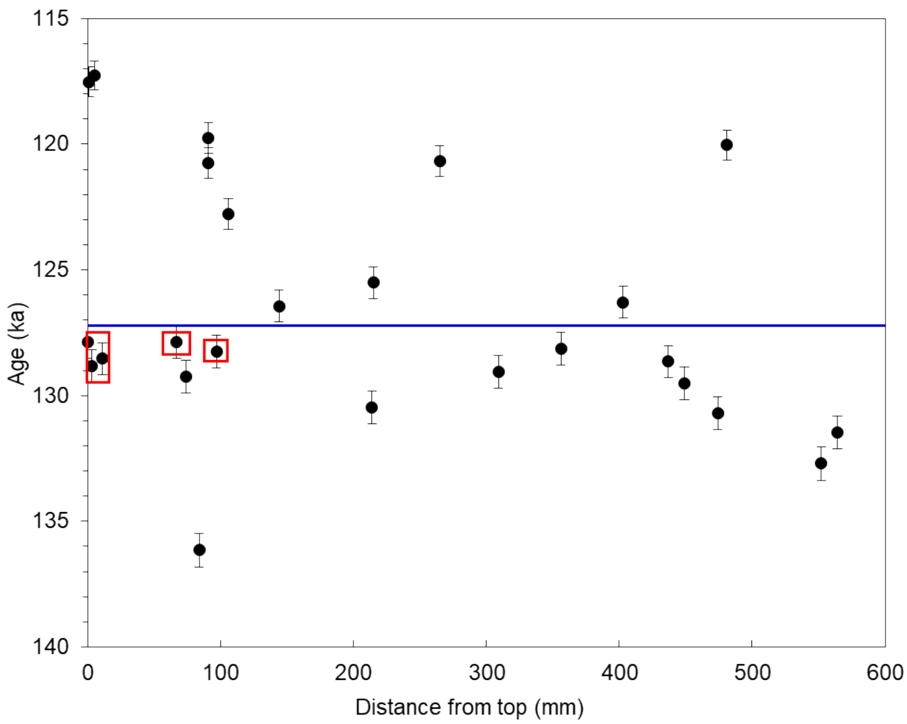

Figure S3. U-Th ages plotted against depth below stalagmite top. The dates cluster around MIS 5e but are not in stratigraphic order, implying disruption in the uranium decay chain in some samples. Boxes enclose 52-series aragonite sample ages, which are considered reliable (see text and Table 1). Dates above the horizontal line are younger than the aragonite dates near the stalagmite top and are therefore rejected from the age model, as is the date of 136 ka which is clearly an outlier.

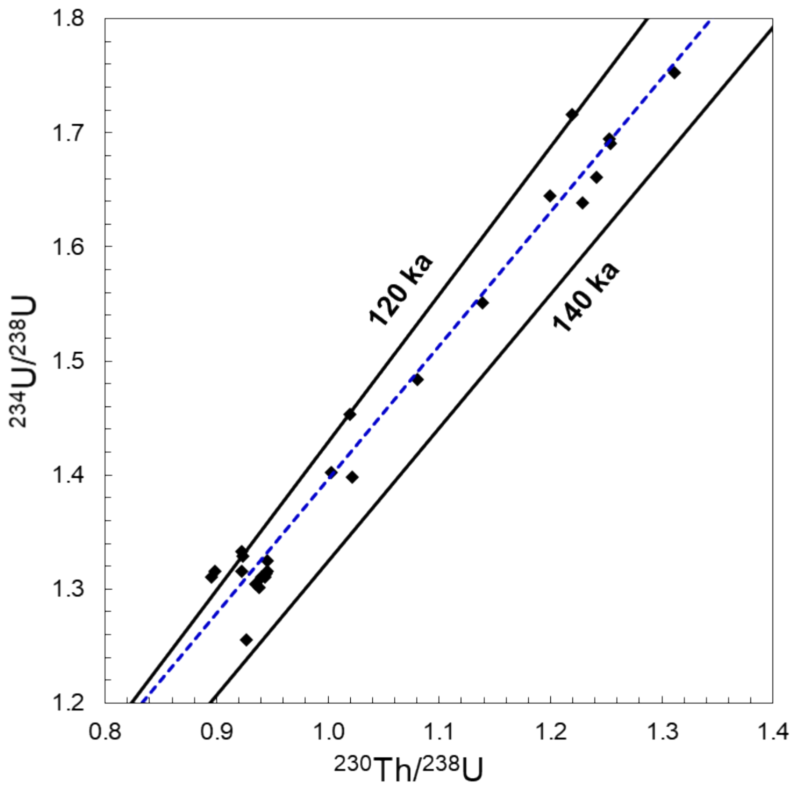

Figure S4. Dim 1 U-series data plotted in $^{234}U/^{238}U$ vs. $^{230}Th/^{238}U$ space. All except two points fall within, or overlap at 2σ, the space between 120 ka and 140 ka isochrons. Blue dashed line is a least squares regression through the data ($R^2 = 0.98$). 2σ error bars lie within the data points.

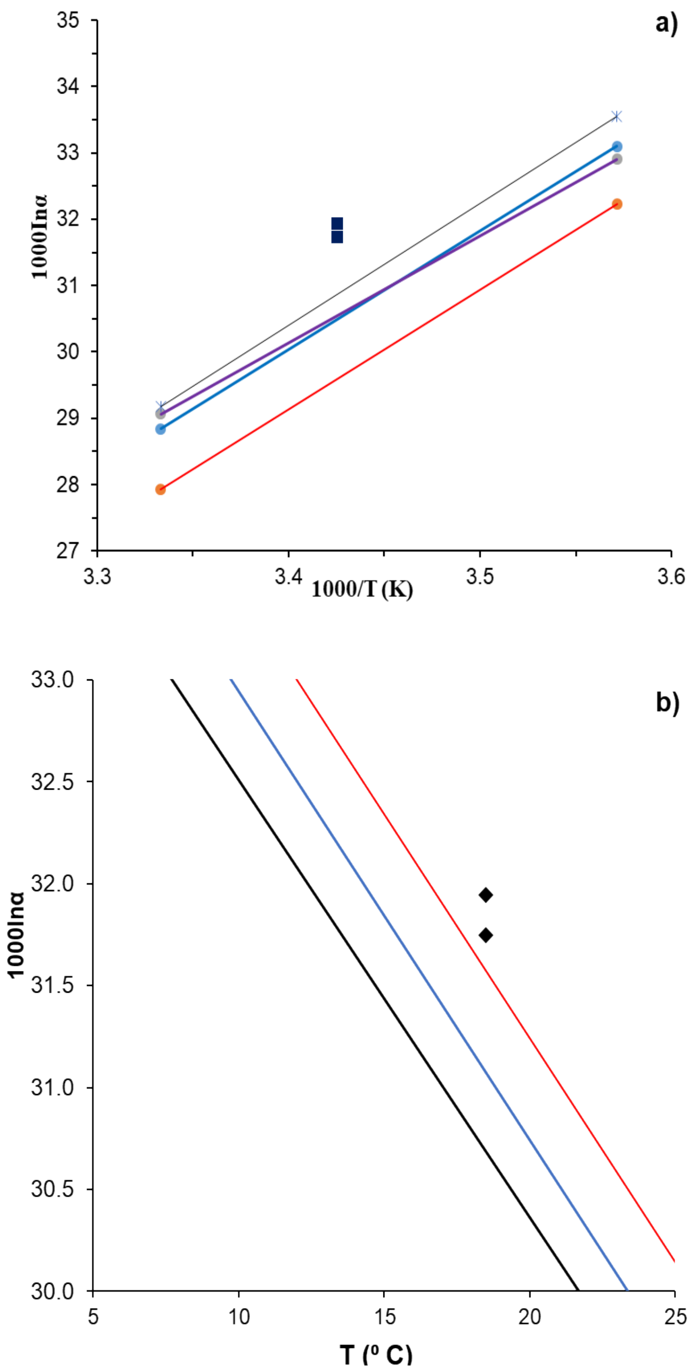

Figure S5. (a) Aragonite-water equilibrium fractionation lines. Blue: (Kim et al., 2007) corrected for acid fractionation factor (Lachniet, 2015); black (Grossman and Ku, 1986). Red line is calcite-water equilibrium fractionation line (Kim and O'Neil, 1997). Purple line is empirical speleothem calcite-water equilibrium fractionation line (Tremaine et al., 2011), offset from the experimentally derived Kim and O'Neil (1997) line. Blue squares are stalactite straws from Dim Cave; (**b)** Aragonite equilibrium equations plotted as 10^3 In α vs. temperature. Black line: 1000Inα $_{\text{aragonite-water}}$ = 17.88±0.13 (10^3/T) - 30.76±0.46 (Kim et al., 2007); blue line: $1000\ln\alpha_{\text{aragonite-water}} = 18.34\ (10^3/T) - 31.954$ (Grossman and Ku, 1986); red line: +0.5‰ upper boundary below which aragonite can be reasonably inferred to have precipitated in, or close to, isotopic equilibrium with its parent water (Lachniet, 2015). Black diamonds show active aragonite stalactites from Dim Cave, which appear to be precipitating out of equilibrium with seepage waters.

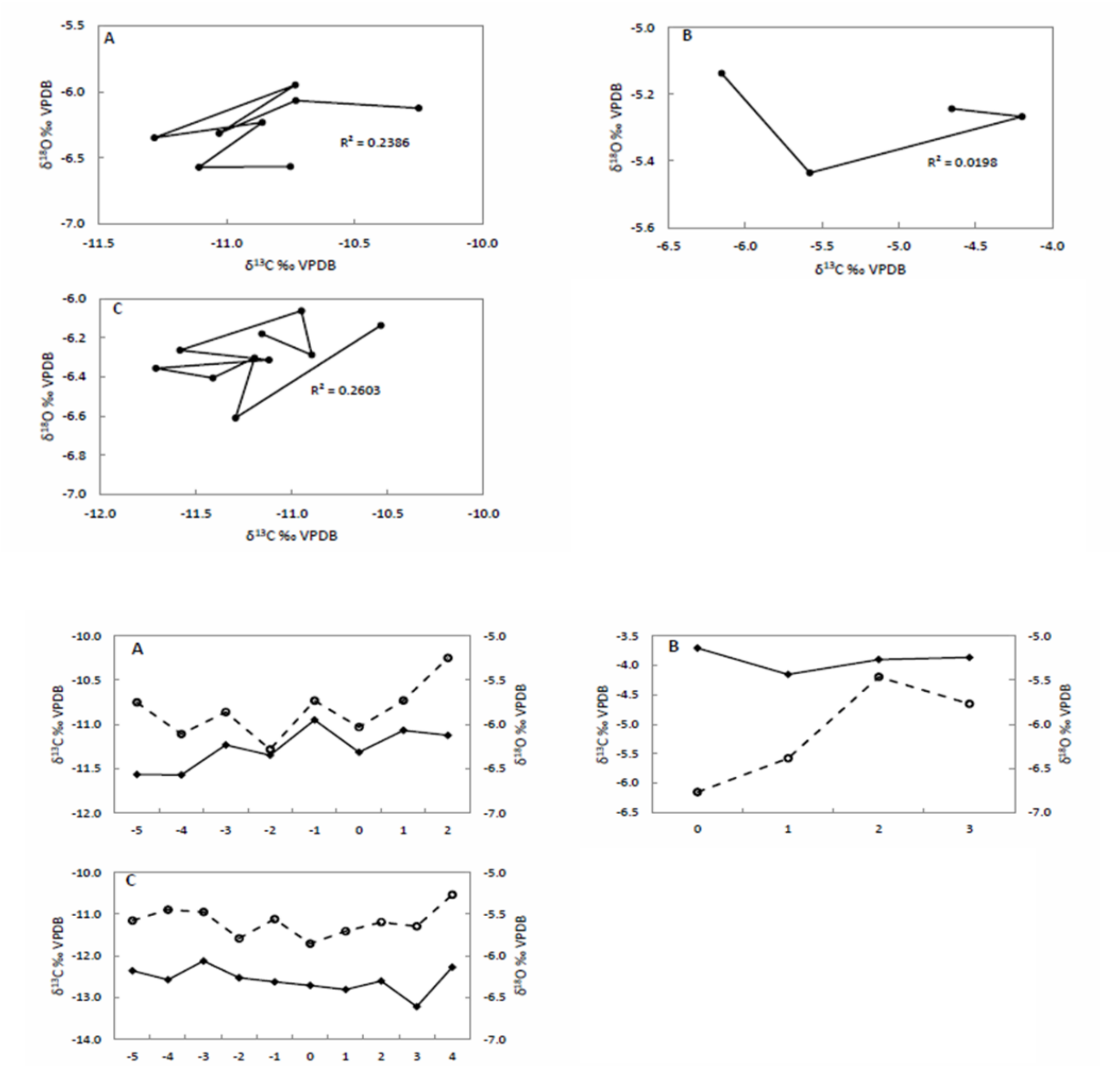

Figure S6. Oxygen and carbon isotope data from Hendy Tests (Hendy, 1971). A: 277 mm, B: 94 mm, C: 22 mm below top. Oxygen and carbon data are poorly correlated, oxygen variability is ≤0.6‰ and there is no systematic enrichment away from the central axis (0 on horizontal axis). Carbon: open circles, dashed line; oxygen: filled diamonds, solid line.

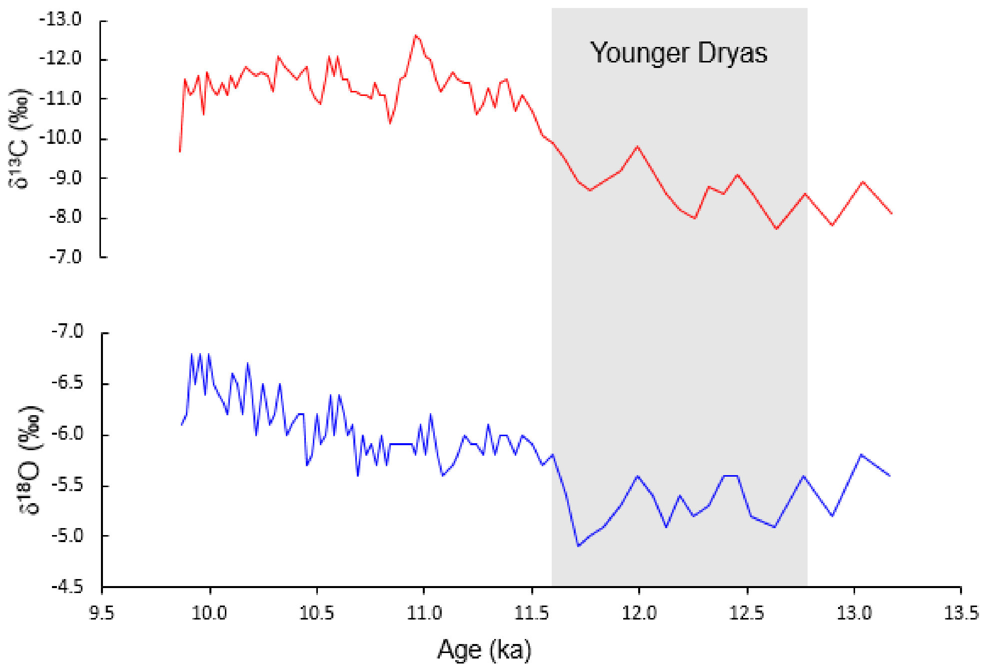

Figure S7. $\delta^{18}O$ and $\delta^{13}C$ records from speleothem Dim-E2 through the last glacial-interglacial transition (Unal-Imer et al., 2015). The $\delta^{13}C$ values and general structure of the record are similar to that part of Dim 1 below the positive isotope excursion. The $\delta^{18}O$ values, however, are consistently less negative by ≥0.5‰ than in Dim 1 below the excursion, and the isotopic pattern has a simpler expression. The magnitude of the Dim 1 $\delta^{18}O$ positive anomaly is similar to the difference between YD and early Holocene values in Dim-E2, and that of the $\delta^{13}C$ is much larger. The YD and the Dim 1 anomaly occupy different chronological positions in the deglacial sequences and are not equivalent, but the comparison suggests that the anomaly records a significant climatic event.

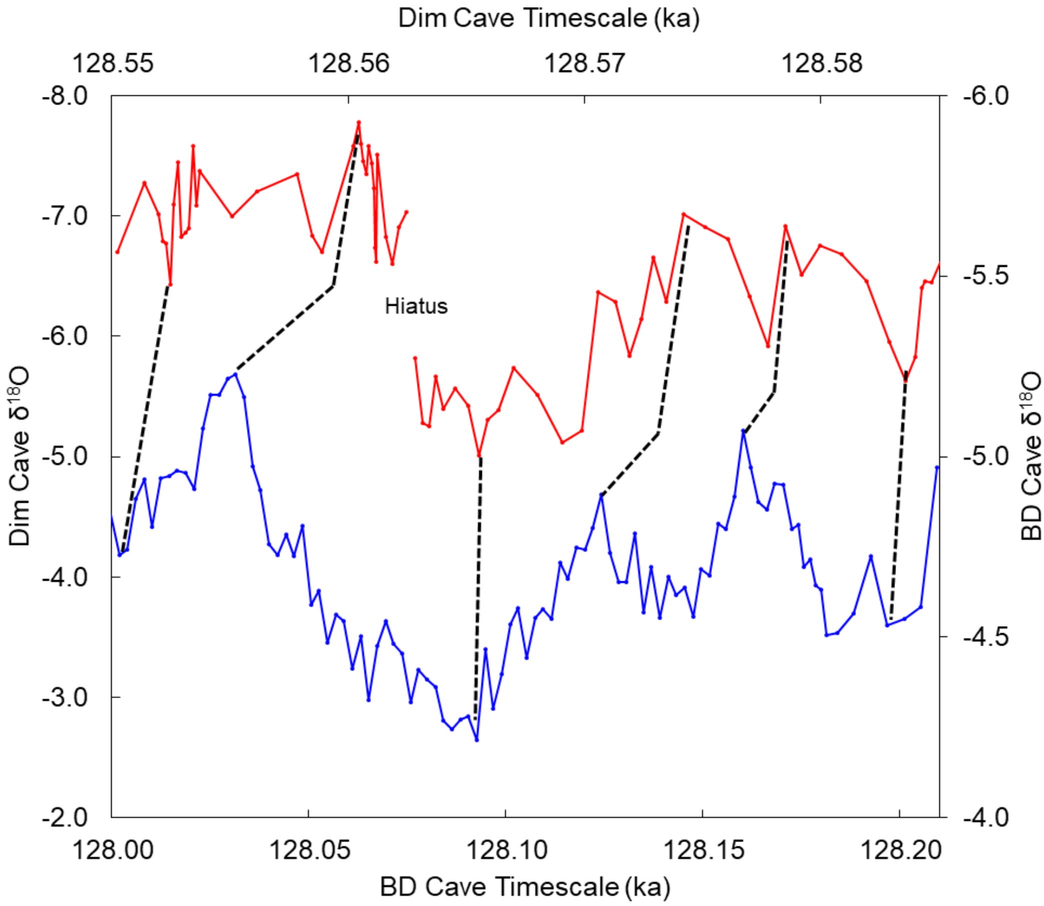

Figure S8. Positive oxygen isotope anomalies in Dim 1 and BDinf plotted on their own timescales. The age offset is ~500 years and lies within the typical 2 s.d. error of the Dim 1 U/Th dates (±~700 years). Strong similarities are evident between the isotopic patterns and dashed lines connect inferred congruent data points. The Dim 1 age model compresses the data into an improbably short time period around the discontinuity whereas the BDinf timescale is more realistic and also closely agrees with the Schneckenloch Cave age model (Fig. 12) (Moseley et al., 2015).

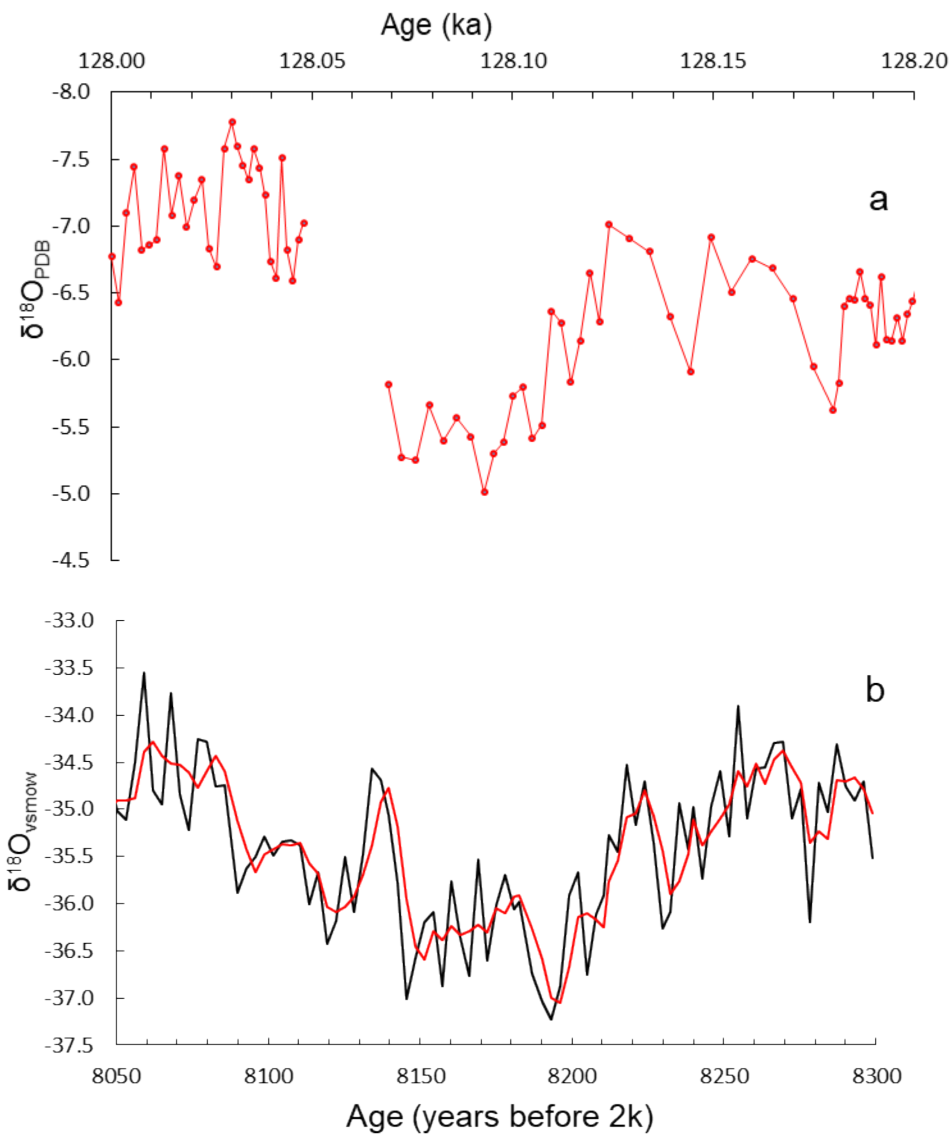

Figure S9. (a) Dim 1 $\delta^{18}O$ positive anomaly plotted on the Bourgeois-Delaunay Cave timescale (Couchoud et al., 2009); (b) Greenland ice core $\delta^{18}O$ negative anomaly at 8.2 ka (Thomas et al., 2007). Heavy line is 3-point running mean. The Greenland "8.2 ka event" is detected globally in stalagmite $\delta^{18}O$ data (Cheng et al., 2009b) as a consequence of abrupt regional changes in temperature or rainfall. The architecture of the two data sets is broadly similar and they occupy comparable timespans of ~200 years, although the Greenland event occurs later in the interglacial. Changes in North Atlantic circulation, especially the MOC, are directly implicated in the Greenland and speleothem 8.2 ka isotopic anomalies and it seems likely that similar events occurred early in previous interglacial periods.

Supplementary References

Anderson, M. B. et al., (2008). High precision U-series measurements of more than 500,000 year old fossil corals. *Earth Plan. Sci. Lett*., **265**, 229-245.

Ayalon, A., Bar-Matthews, M., Kaufman, A. (1999). Petrography, strontium, barium and uranium concentrations, and strontium and uranium isotope ratios in speleothems as palaeoclimatic proxies; Soreq Cave, Israel. *The Holcene*, **9** (6), 715-722.

Cheng, H., Edwards, R. L., Hoff, J., Gallup, C., D. Richards, D. A., Asmerom, Y. (2013). The half-lives of uranium-234 and thorium-230. *Chemical Geology*, **169**, 17-33.

Craig, H. (1961). Isotopic variations in meteoric waters. *Science*, **133**, 1702.

Gat, J.R. and Carmi, I. (1970). Evolution of the Isotopic Composition of Atmospheric Waters in the Mediterranean Sea Area. J. *Geophys. Res*., **75**, 3039-3048.

Goede, A., McCulloch, M., McDermott, F., Hawkesworth, C. (1998). Aeolian contribution to strontium and strontium isotope ratios variations in a Tasmanian speleothem. *Chemical Geology*, **149** (1-2), 37-50.

Hiess, J., Condon, D. J., McLean, N., Noble, S. R. (2012). $^{238}U/^{235}U$ systematics in terrestrial uranium-bearing minerals. *Science,* **335**, 1610-1614.

Verheyden, S., Keppens, E., Fairchild, I. J., McDermott, F., Weis, D. (2000). Mg, Sr and Sr isotope geochemistry of a Belgian Holocene speleothem: implications for palaeoclimate reconstructions. *Chemical Geology*, **169**, 131-144.